EFFECTS OF REBAR TEMPERATURE AND WATER TO CEMENT RATIO ON REBAR-CONCRETE BOND STRENGTH OF CONCRETE CONTAINING FLY ASH

Ardeep Ranjan Pati B. E.

Thesis Prepared for the Degree of

MASTER OF SCIENCE

UNIVERSITY OF NORTH TEXAS

May 2010

APPROVED:

Seifollah Nasrazadani, Major Professor
Phillip R. Foster, Committee Member
Cheng Yu, Committee Member
Reza Mirshams, Committee Member
Nourredine Boubekri, Chair, Department of Engineering Technology
Costas Tsatsoulis, Dean of the College of Engineering
Michael Monticino, Dean of the Robert B. Toulouse School of Graduate Studies

Pati, Ardeep Ranjan. Effects of Rebar Temperature and Water to Cement Ratio on Rebar-Concrete Bond Strength of Concrete Containing Fly Ash. Master of Science (Engineering Systems), May 2010, 77 pp., 11 tables, 40 figures, references, 48 titles.

This research presents the results on an experimental investigation to identify the effects of rebar temperature, fly ash and water to cement ratio on concrete porosity in continuously reinforced concrete pavements (CRCP). Samples were cast and analyzed using pullout tests. Water to cement ratio (w/c) and rebar temperature had a significant influence on the rebar-concrete bond strength. The 28-day shear strength measurements showed an increase in rebar-concrete bond strength as the water to cement ratio (w/c) was reduced from 0.50 to 0.40 for both fly ash containing and non fly ash control samples. There was a reduction in the peak pullout load as the rebar surface temperature increased from 77° F to 150° F for the cast samples. A heated rebar experiment was performed simulating a rebar exposed to hot summer days and the rebar cooling curves were plotted for the rebar temperatures of 180°F-120° F. Fourier transform infrared spectroscopy was performed to show the moisture content of cement samples at the rebar-concrete interface. Mercury intrusion porosimetry test results on one batch of samples were used for pore size distribution analysis. An in-depth analysis of the morphological characteristics of the rebar-concrete interface and the observation of pores using the scanning electron microscope (SEM) was done.

ACKNOWLEDGEMENTS

It is with heartfelt gratitude that I would like to express my appreciation to my committee chair, Dr. Seifollah Nasrazadani for his guidance and support throughout my graduate program and in the completion of this thesis project. I would also like to thank my committee members Dr. Phillip Foster, Dr. Cheng Yu, and Dr. Reza Mirshams for their assistance, careful reading and the suggestions they provided at all levels of this thesis project.

To my family, thank you for your support and encouragement throughout my studies in America. Thank you for your patience, confidence and for believing in me, words cannot express how much you are appreciated. I must acknowledge my parents Mr. and Mrs. Arabinda Pati for encouraging us as family to always shoot for the stars, for their constant moral, spiritual and financial support. Thank you and God bless you abundantly. Finally yet importantly, I would like to thank all my dear friends whose names cannot fit this space for all their support and encouragement, you guys are the greatest and I am blessed to have all of you share and experience this wonderful life that we have been blessed to have. It has been a bumpy and rough ride, we neither lost our faith nor focus and we are finally making it!

This research project is sponsored by Federal Highways Administration and Texas Department of Transportation through Project 0-5549. I am thankful for the support I received in this project.

TABLE OF CONTENTS

Page

LIST OF TABLES

LIST OF FIGURES

CHAPTER 1

INTRODUCTION

The state of Texas first used continuously reinforced concrete pavements (CRCP) in 1951 on two contiguous projects in Fort Worth, Texas. Because of these pavements' outstanding performance, the Texas Department of Transportation (TxDOT) continued to construct many roads using CRCP. Texas is now the leading state in lane miles of CRCP. Significant technical and design development in the construction of CRCP has made concrete paving faster, less expensive, and more durable. CRCP is a Portland cement concrete (PCC) pavement that has continuous longitudinal and transverse steel rebar reinforcement and no intermediate transverse expansion or contraction joints (Figure 1). The function of the longitudinal steel is not to strengthen the concrete slab, but to control concrete volume changes due to temperature and moisture variations and to keep transverse cracks tightly closed (TxDOT Pavement Design Guide 2006). The function of the transverse steel is to keep longitudinal joints and cracks closed. CRCP was first constructed in Indiana and Illinois in the 1930s and 1940s. According to the Transportation Research Board (Robinson, 1996) a lack of attention to design and construction details has caused premature failures in some CRCPs. The causes of early distress have usually been traced to:

(1) Construction practices which resulted in pavements which did not meet design requirements

(2) Designs which resulted in excessive deflections under heavy loads

(3) Bases of inferior quality,

(4) Combinations of these or other undesirable factors

Figure 1. Continuously reinforced concrete pavement. Courtesy Concrete Reinforcing Steel Institute

The presence of continuous reinforcement makes it difficult for cracks to initiate and propagate. Distresses in CRCP has however been observed in Texas, Illinois and Virginia due to horizontal cracking of the pavements. This does not only lead to the costly repairs of the roads but also results in the reduction of the useful life of the concrete pavements.

Problem Statement

Texas Department of Transportation (TxDOT) decided to use CRCP as the primary PCC pavement type because of the excellent performance history of CRCP, which include high durability and strength characteristics. Even though the performance of CRCP in Texas

has been excellent, some sections have had to be rehabilitated before their design lives were reached. According to Transportation Research Board (Robinson, 1996) two major distresses in CRCP in Texas are punchout and spalling. Spalling is a surface distress and rarely presents a structural distress. It is also well understood that spalling has more to do with the coarse aggregate type used in concrete. Therefore, the only structural distress in CRCP is punchout. Punchout is a serious distress which needs to be repaired as soon as possible since un-repaired punchout can cause a safety hazard to the traveling public. To address the punchout issues, the TxDOT made a few changes in the mid-1980s, which included the use of thicker concrete slabs, stabilized subbase (either 6-in cement stabilized base or 4-in asphalt stabilized base) and tied concrete shoulders. These changes have been effective, in substantially reducing the frequency of punchout. However, during the full-depth repair of what appeared to be punchout, it was observed that there was a different form of punchout, which the above three changes did not appear to alleviate. Further evaluation of this form of distress revealed that this distress is caused by horizontal cracks in concrete at the depth of close to the longitudinal steel (mid-depth of the slab).

Delaminations at the steel depth have been observed in some CRCP in the past. This type of delamination is attributed to several factors. Some projects were paved in a two-stage construction process, placing steel on top of the first layer of concrete in plastic state, and then constructing the second layer immediately following this. In some cases, delamination was observed due to a delay in placement of the second layer. After the concrete slab has delaminated, it separates into two layers at the depth of reinforcing steel. The axle loading is carried by the upper layer, making it easy to break, particularly

in the wheel path of trucks. Following proper curing guidelines and techniques and careful selection of the aggregate can minimize the occurrence of delaminations.

Corrosion of steel rebar in concrete is also another factor which could potentially lead to horizontal cracking along its plane. This may lead to spalling of concrete cover. The important factors in corrosion of steel rebar in concrete are the volume of oxides and where it is formed. The main problem is that the pore water is static and there is no transport mechanism to move the oxide away from the steel surface. The dense oxide formed at high temperatures gets deposited at metal oxide interface. Edges of the concrete slab structures tend to crack first on corroding. Delaminations occur as corrosion proceeds on neighboring rebars and horizontal cracking takes place (Broomfield, 1997). The engineering properties of concrete such as permeability, shrinkage, strength and durability are determined by the number, type and size of pores. The strength and elasticity is affected by the total volume of pores whereas concrete permeability is affected by the pore volume, size and continuity (Md. Safiuddin, 2005).

Although many reasons for horizontal cracking in CRCPs has been mentioned (M. Won, 2004), there has been no mention of the effect of rebar temperature on rebar-concrete bond strength. Rebar-concrete bond formation at different water to cement ratios and rebar temperature produces vastly different bond strengths. Hence an in depth research is to be done to understand the relationship between rebar temperature, water to cement ratio and the concrete rebar bond quality. Understanding the porosity of cement at the rebar concrete interface will facilitate an understanding of the micro structural factors responsible for horizontal cracking in CRCP.

Purpose of Research

Purpose of this research is to investigate effects of rebar temperature, water to cement ratio and inclusion of fly ash in concrete mix on rebar-concrete bond strength. Rebar temperatures between 120 ^{o}F – 180 ^{o}F (to simulate CRCP construction in a typical Texas hot summer day) will be used to determine the thermal effect on the cement porosity at the rebar-concrete interface. Hot weather placement has been known to cause the formation of erratic crack spacing, including y-cracking, narrow crack spacing, and crack intersections (Concrete Reinforcing Steel Institute). Given these conditions, punchouts can develop rapidly and result in a significant increase in pavement repairs and maintenance. Rebar-concrete bonding strength will be measured using a group of ASTM standard cylinders cast (with embedded rebar) samples made at rebar temperatures of 77^{o}F and 150^{o}F with plain rebars. These samples were divided into fly ash containing and regular Portland cement which were used during the preparation process. Pullout test were performed on cast samples to evaluate bonding strength and rebar-cement interface characteristics were studied using scanning electron microscopy. The ultimate goal of this research is to understand the effect of rebar temperature and water to cement ration on rebar-concrete bonding strength. These factors potentially influence the horizontal cracking in CRCP. Attempts are made to recommend modifications to Pavement Design Guide for CRCP construction practices of Texas Department of Transportation.

Statement of Need

Due to initial costs incurred during the construction of the concrete pavements, preventive measures should be taken to prevent the occurrence and propagation of

horizontal cracks which ultimately lead to expensive full depth repair of the concrete pavements. Currently Texas has about 9,400 lane miles of pavement on which TxDOT spends more than 50% of the annual construction and maintenance budget (TxDOT Pavement Design Guide, 2006). The design and construction quality control in CRCP is not only critical for the service life of pavements, but also for the safety of the road users. In long run the drivers may see benefits if their vehicle requires less repairs from pothole damages and possibly better fuel mileage from smoother surfaces.

The findings in this research should help in minimizing the horizontal cracking in pavements which lead to the formation of potholes and half depth punch-outs. This will ensure increased public safety and the cost of repairs on the CRCP can also be minimized. It will save money in not just man hours, but also materials and testing time, which in turn end up costing everyone less.

Research Questions

1. What is the effect of rebar temperature and water to cement ratio on rebar-cement bond strength?
2. Is the porosity and pore size distribution in the vicinity of rebar-concrete related to bond strength?
3. What effect does addition of fly ash to Portland cement have on the concrete-rebar strength?

Assumptions

1. Pullout test apparatus treated each sample in the same manner and replicated environment as encountered in the field of CRCP construction.
2. The heating rebar apparatus replicated heat absorption/dissipation environment encountered in the field of CRCP construction.

Terminologies

ASTM – American Society of Testing Materials

CRCP – Continuously reinforced concrete pavements

EDS – Energy dispersive spectroscopy

FRP – Fiber reinforced polymer

FTIR – Fourier transform infrared spectroscopy

MIP – Mercury intrusion porosimetry

PCC – Portland cement concrete

SEM – Scanning electron microscopy

TxDOT – Texas Department of Transportation

CHAPTER 2

REVIEW OF LITERATURE

According to the paper published by Kim and Won (2004) horizontal cracking was first observed in the continuously reinforced concrete pavements (CRCP) section of IH-30 in the Paris district in Texas. The typical distress types included popouts and half-depth punchouts as shown in Figure 2(a). During a repair work, extensive horizontal cracks were observed in the removed slabs as shown Figure 2(b). On close examination of these horizontal cracks, the cracks occurred around the coarse aggregates, not through the aggregates, which is an indication of early age cracking. On IH-35 in the Waco district, horizontal cracks at the depth of reinforcing steel were observed in a relatively new CRCP that was not yet open to traffic. These cracks were observed to initiate and propagate from the mid section where the rebar steel placement is done (Figure 2.c) and in some cases propagate throughout the road width (Figure 2.d).

Figure 2. Horizontal cracking distresses in CRCP (a), Mid-depth bond failure (b, c), Extension of horizontal cracks covering total road width (d). Courtesy of the Center of Transportation Research, University of Texas at Austin).

Kim and Won (2004), expressed the following features of horizontal cracking:

- Shear stress in slabs has a parabolic distribution, with the highest stress at mid slab, which could explain the delamination at that location.
- The curling action of the concrete due to drying and temperature changes may be the most significant contributor to horizontal cracking in CRCP.
- The dissimilarity between the reinforcing steel and the concrete in thermal and drying shrinkage may be a contributory factor in causing the delamination to be located at the level of the steel.
- The selection of ingredients and their proportioning affect the shrinkage curling. After the concrete slab has delaminated, it separates into two layers at the reinforcing steel. Now, the axle loading is carried by the upper layer, making it easy to break mainly in the wheel path of truck.

In their theoretical analysis to estimate the effects of several design, environmental, and materials variables (number of steel layers, temperature variations, and thermal coefficient of thermal expansion and modulus of elasticity of concrete) on the potential for horizontal cracking, Kim and Won (2004) utilized a finite element modeling as shown in Figure 3. They based their analysis on horizontal cracking observed in Texas.

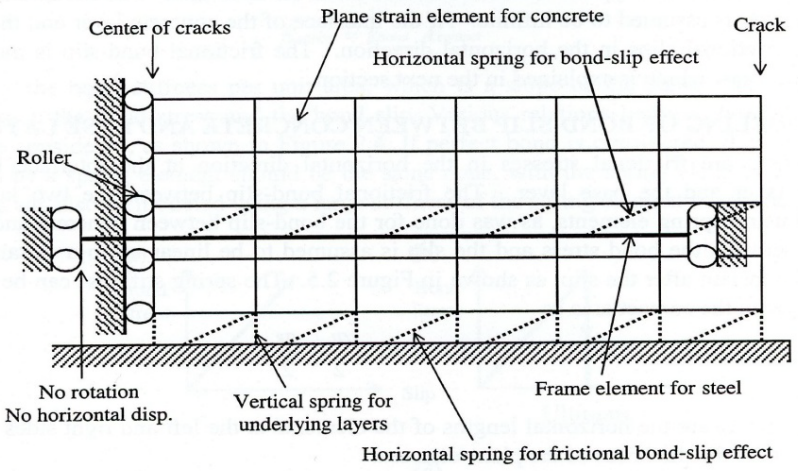

Figure 3. Finite element model of CRCP (Kim & Won, 2004).

They introduced bond slip element to model the interface between concrete and longitudinal steel with the assumption that concrete behaved in plane strain mode. They found that higher temperature differentials between the top and bottom of the slab resulted in larger concrete stresses at the depth of steel. The finite element modeling used by Kim and Won (2004) is not sophisticated enough to provide quantifiable relationships, which could be used to develop design standards or specifications to mitigate horizontal cracking.

There was research done to experimentally investigate the significant factors influencing concrete/rebar bond failures resulting in cracking of CRCP. Nasrazadani and Sudoi (2008) studied the effects of water to cement ratio, rebar temperature at the time of concrete pouring and rebar surface condition (corroded vs. non-corroded) on pullout bond strength of CRCP and concluded that:

1. The presence of corrosion products on the rebar-concrete interface ultimately led to a reduction on rebar concrete bond strength, but corrosion cannot be said to be responsible for early age cracking as microcracks were also observed on the non-corroded rebar specimens at as early as three days.
2. The lower the water to cement ratio the higher the rebar concrete bond strength.
3. There was a reduction in the peak pullout load as the temperature is increased for both the corroded and non-corroded rebar experiments.

The porosity of the cement at rebar-concrete interface was not taken into consideration in any of the researches mentioned above which could lead to the degradation of rebar-concrete bond strength and hence it needs to be investigated in this research.

Concrete technology has made numerous advancements in all areas including materials, mixture proportioning, recycling, structural design, durability requirements, and testing and specifications. High performance concrete mixtures have developed that includes recycled materials like fly ash (FA). In recent years ultra fine powders like fly ash have become necessary ingredients of high-performance concrete as they improve the properties of hardened concrete. Addition of fly ash increases the fluidity of fresh concrete representing the water-reducing effect (Wei, 2003). Application of recycled materials like FA in concrete production has huge positive environmental impact by reducing CO_2 emission, energy consumption, and in turn reducing global warming. Typically concrete containing recycled materials are used to construct pavements. Two common FA classes include Class C and Class F. Both classes contain SiO_2, Al_2O_3, and

Fe_2O_3. While sum of these constituents in Class C must exceed 50% Class F is required to have a total of more than 70%. Both of these materials exhibit Pozzolanic activity. Currently about 41.4% of Class C and 75.1% Class F FA available in the state of Texas contributes to landfill.

Addition of FA to concrete materials is proven to increase compressive strength of cement profoundly. Oner (2005) showed that compressive strength of cement measured at 28 days of setting was increased by addition of fly ash and its optimal amount was shown 40%. Seddique (2003), studied effects of 10%, 20%, 30%, 40%, and 50% of Class F fly ash by weight and found a significant improvements of mechanical properties as the result of fly ash addition. Fu and her colleagues (2002) also arrived at the same conclusions as previous investigators that addition of large amounts of fly ash will enhance mechanical properties of concrete. Laguros (1984) used x-ray diffraction and scanning electron microscopy (SEM) to study concretes containing fly ash and showed retardation of setting are directly proportional to the amount of fly ash replacing Portland cement.

According to Estakhri and her colleagues (2004), from 18 power plants located throughout the state of Texas 6.6 million tons of fly ash will be produced annually in Texas and 40% of that is used in concrete. This group suggested that if 60% of the Portland cement used in Texas concrete production were replaced with fly ash, carbon dioxide emission could potentially be reduced by 6.6 million tons annually by the year 2015. This reduction would have a sizable impact on environment and potential cost reduction savings from environmental issues. It is striking to know that that one ton of

carbon dioxide is produced for production of one ton of cement products and therefore for every ton of FA replacement with Portland cement one expects to reduce one ton of carbon dioxide. Estakhri's group also sited two barriers for applications of FA in cement. According to them, high cost of additional silo (1 million dollars per silo) for concrete makers, and maximum 35% allowable FA in concrete by TXDOT and many other agencies are the two main barriers for application of fly ash. It must also mentioned technical issues like setting time delay due to addition of FA in concrete needs to be considered as another barrier. Technical issues involved with FA use can be studied and proper course of actions can be taken to minimize these concerns. Many investigators in the past studied cements and concretes using conventional SEM (Wei, 2003).

Steel has an expansion coefficient nearly equal to that of modern concrete. If this weren't so, it would cause problems through additional longitudinal and perpendicular stresses at temperatures different than the temperature of the setting. Although rebar has ribs that bind it mechanically to the concrete, it can still be pulled out of the concrete under high stresses, an occurrence that often precedes a larger-scale collapse of the structure. To prevent such a failure, rebar is either deeply embedded into adjacent structural members (40-60 times the diameter), or bent and hooked at the ends to lock it around the concrete and other rebar. This first approach increases the friction locking the bar into place, while the second makes use of the high compressive strength of concrete.

Common rebar is made of unfinished tempered steel, making it susceptible to rusting. One can see clearly the pearlite and ferrite phases in the microscopic analysis of the steel rebar surface (Figure 4). Normally the concrete cover is able to provide a pH value higher

than 12 avoiding the corrosion reaction. Too little concrete cover can compromise this guard through carbonation from the surface. Too much concrete cover can cause bigger crack widths which also compromises the local guard. As rust takes up greater volume than the steel from which it was formed, it causes severe internal pressure on the surrounding concrete, leading to cracking, spalling, and ultimately, structural failure. This is a particular problem where the concrete is exposed to salt water, as in bridges built in areas where salt is applied to roadways in winter, or in marine applications.

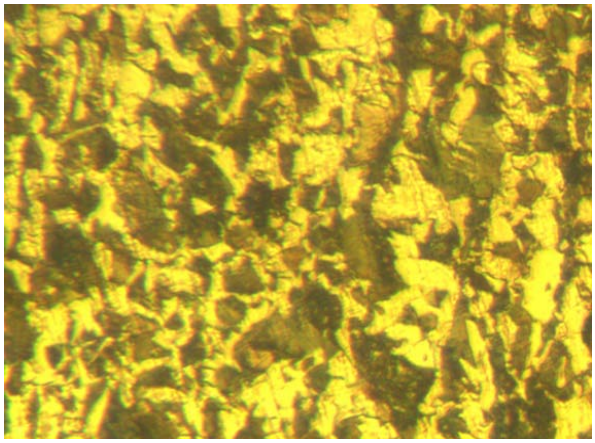

Figure 4. Optical micrograph of phases present in rebar steel showing pearlite (dark phase) and ferrite (light phase) at 200X magnification.

In recent years, the corrosion of reinforcing steel rebars in concrete systems, has gained considerable attention. Reinforcing rebars having higher corrosion resistances compared to the common carbon-steel rebars can be used to provide more protection against corrosion in aggressive environmental conditions or when a long service life is required. The corrosion resistance of rebars can be increased either by modifying the chemical composition of the steel rebars or by applying a metallic or organic coating on to the surface of such rebars. Three families of reinforced rebars have commonly been

used in reinforced concrete structures to protect against corrosion, namely stainless-steel, galvanized-steel and epoxy-coated rebars (Bertolini L, 2004). Fiber-reinforced polymer (FRP) rebars consisting of an epoxy matrix with carbon or aramide fiber have been proposed as a possible replacement but are still in experimental phase and there is a lack of experience on their durability.

There are also some disadvantages associated with the main rebar types that are currently being used. For example stainless-steel bars are much more expensive than the carbon steel ones. Galvanized-steel rebars, in addition to being high priced due to the high price of galvanizing process, have the further disadvantage of having an exponentially increased rate of corrosion at pH values above 13.3. The reactions between metallic zinc and the hydration products may affect the bond strength between the galvanized-steel and the concrete. Requirements for epoxy-coated reinforcing bars are reported in international standards. Although the price of epoxy-coated bars is higher than uncoated bars, the main problem is the reduction of bond strength between the epoxy-coated rebars and the concrete. Therefore some design procedures such as increasing the splice length have been developed to account for this influence (M.M. Jalili, 2006).

Rebar is available in different grades and specifications that vary in yield strength, ultimate tensile strength, chemical composition, and percentage of elongation.

The grade designation is equal to the minimum yield strength of the bar in ksi (1000 psi) for example grade 60 rebar has minimum yield strength of 60 ksi. Rebar is typically manufactured in grades 40, 60, and 75.

Common specifications are:

- ASTM A 615 Deformed and plain carbon-steel bars for concrete reinforcement
- ASTM A 706 Low-alloy steel deformed and plain bars for concrete reinforcement
- ASTM A 955 Deformed and plain stainless-steel bars for concrete reinforcement
- ASTM A 996 Rail-steel and axle-steel deformed bars for concrete reinforcement

CHAPTER 3

EXPERIMENTAL PROCEDURES

Analysis of Cast Samples

Specimen Preparation

Laboratory test specimens were prepared as per ASTM Standard C 192/C 192M-00 “Standard test method for comparing concretes on the basis of the bond developed with reinforcing steel.” Cylindrical casts with a diameter of 4 in x 8 in. length were used for this experiment (Figure 5). The cylindrical casts were made from concrete test cylinder molds conforming to ASTM 470 standard. These dimensions were chosen because they are lightweight, small, consume less material and require lower area for curing period. The embedment length was 8 inches.

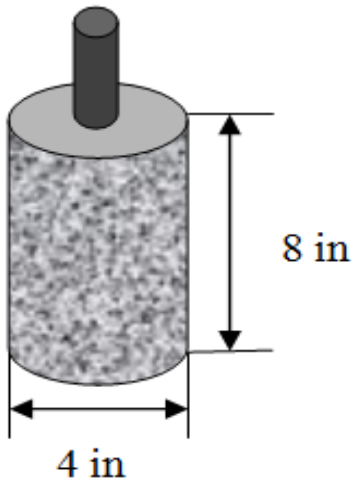

Figure 5. Cast rebar specimen for pullout strength analysis

The rebar steel, used for this experiment, was in accordance to ASTM A615 "Standard specification for deformed and plain billet-steel bars for concrete reinforcement." The # 6 bar properties used are shown in Table 1.

Table 1. ASTM A615 Requirements (American Society for Testing and Materials, Pennsylvania, 2001).

Rebar Specifications			
Bar Size	Nominal Weight (lb/ft)	Nominal Diameter (in)	Cross-sectional area ($in.^2$)
6	1.502	0.75	0.44

Mix Proportions

The selection of a good concrete mix proportion is essential for the achievement of a balance between economy, placement requirements, durability, density, appearance and strength of the concrete mix. The bulk specific gravity and absorption capacity of the materials used in this research are shown in Table 2.

Table 2. Bulk specific gravity and absorption capacity of materials.

Material	**BSG***	**AC*** (%)**	**Description**
Cement	3.15	NA	Type I/II
Water	1	NA	
Rock	2.65	2	Estimate, Crushed LS**
Sand	2.6	1	Estimate, Natural Sand
* BSG = Bulk Specific Gravity. **LS=Limestone *** AC = Absorption Capacity.			

The batch weights were calculated for the preparation of 54 specimens for each experimental run. These w/c ratios were chosen based on common CRCP construction practices. The w/c ratio chosen for the construction purpose is optimized to achieve the required strength, durability and permeability requirements.

Volume per mold sample = 100.43 in^3

Individual w/c ratio samples to be cast for the 10 and 28 day tests: 0.40 = 36

0.45 = 36

0.50 = 36

Total volume in yd^3 for each w/c: = 0.08yd^3

The batch mix requirements for the experiment are shown in Tables 3 and 4.

Table 3. Batch mix requirements for the fly ash mix concrete.

	W/C 0.40	W/C 0.45	W/C 0.50
Water (lbs)	18	20	22
Cement (lbs)	30	30	30
Coarse aggregate (lbs)	170	170	170
Fine aggregate (lbs)	112	112	112
Fly ash (lbs)	16	16	16

Table 4. Batch mix requirements for the non fly ash mix concrete.

	W/C 0.40	W/C 0.45	W/C 0.50
Water (lbs)	18	20	22
Cement (lbs)	46	46	46
Coarse aggregate (lbs)	170	170	170
Fine aggregate (lbs)	112	112	112

Table 5 shows the experimental run matrix for the 8-in embedment length experiments for the fly ash mix and non-fly ash mix concrete.

Table 5. Experimental run matrix for the 8-in embedment length experiments for the fly ash mix and non-fly ash mix concrete.

Run @ 3 specimens per run	W/C	Temperature (^{o}F)	Embedded Length (in)
1	0.40	77	8
2	0.40	77	8
3	0.40	77	8
4	0.45	77	8
5	0.45	77	8
6	0.45	77	8
7	0.50	77	8
8	0.50	77	8
9	0.50	77	8
10	0.40	150	8
11	0.40	150	8
12	0.40	150	8
13	0.45	150	8
14	0.45	150	8
15	0.45	150	8
16	0.50	150	8
17	0.50	150	8
18	0.50	150	8

Total number of samples per run = 54

Total number of samples for the 10 and 28 day tests = 108 {with pozzolan additives}

=108{without additives for control}

Rebar Temperature Control

The rebar temperatures were chosen to simulate normal/ambient conditions and hot summer days. This simulated rebar temperature condition during the concrete placement stage. The normal/ ambient temperature condition, 77 ^{o}F, is an approximate room temperature and did not require any adjustment on rebar temperature. The heat flux

intensity of the sun is 700 w/m^2 (Yunus, 2003). In summer time the duration of the day is from 6 AM to 8 PM approximately in Texas which leads to very high rebar temperatures. Simulating extreme summer temperature of 150 ^oF was achieved by heating the rebar to the desired temperature in a temperature control oven. Rebar samples were left in the oven for four hours to ensure even heat distribution. Once the desired temperature was reached, the rebar samples were removed and immediately and cast was made around them.

Experimental Program

The experimental program was designed to evaluate the bond strength of the test specimen. The concrete mixes were designed using ordinary portland cement (OPC) Type I/II, sand and aggregates. The effect of the addition of fly ash on the concrete mix together with the influence of the variation of rebar temperature was observed. Control specimens without fly ash mix were cast for comparison. The rebar steel was placed at the center of the cylindrical specimens. The embedment length of 8 inches was maintained for each experimental run. After the specimens were cast, they were covered immediately with a polythene bag to prevent evaporation. The molds were removed after 32 hours of casting and moist cured by spraying with tap water at room temperature until the pullout tests were performed (ASTM Standard C39/C 39M-01, Pennsylvania, 2001).

The pullout tests were conducted at different ages since the bond slip behavior will change depending on concrete strength (bond strength). This allowed for the investigation of the “early age” cracking phenomenon. The pullout tests were done at 10 days and 28 days for the 77 ^oF and 150 ^oF.

Pullout Test Specimen Setup.

The bond-slip relationship was examined using the pullout test. This was done in accordance to the standard RILEM pullout test, AAC 8.1; "Pullout test for reinforcement." This standard was used because the ASTM standard C234 – 91a "Standard test method for comparing concretes on the basis of the bond developed with reinforcing steel," was withdrawn in February 2000 (Manual Book of ASTM Standards, 2001). The pullout test was performed in order to measure the interfacial strength between the rebar and the concrete matrix. The rebar was gripped by the cross head of an Instron 4482 Tensile tester with a maximum tensile load capacity of 20 kips (88 KN). A specially designed loading frame was fixed to the base of the Instron universal testing machine (Figure 6). Advantages of the pullout test include:

1. It offers the advantage of simplicity.

2. The free end of the rod is accessible allowing for the measurement of the free end slip and for the placement of instrumentation.

Figure 6. Pullout test setup

Some of the disadvantages of using this set up however are:

1. Failure by splitting of the concrete mass may occur at a load below the maximum bond capacity.

2. The compressive stresses exist in the concrete near the loaded end of the rod. These compressive stresses at the loading face are however very small and hence are neglected during the pullout test process.

The rebar was gripped at the top by the Instron tester and secured at the bottom by the fabricated steel fixture shown in Figure 6.

Heated Rebar Experiment

High rebar temperature during the process CRCP construction is a major factor which can lead to several distresses as mentioned in the section earlier. Depending upon the rebar temperature, characteristics of rebar-concrete interface may be different. High rebar temperatures causes cement partial drying which makes w/c being lower at the interface compared to the bulk cement. Hence a heated rebar experiment was performed to determine if there is any change in the rebar-concrete interface with respect to the temperature. Simulation of hot summer days when CRCP is constructed was done by heating the rebar to temperature range of 120 ^{o}F to 180 ^{o}F.

In order to simulate concrete placement over rebar steel in a hot summer day, hollow gage 6 rebar steels 6 inch in length with inner hollow diameter of 0.25 in was

prepared. Hollow space was drilled to facilitate insertion of a heating element cartridge which was connected to hp power supply model E3612A. A WATLOW EZ-ZONE temperature controller was placed between the rebar and the power supply to control and regulate rebar surface temperature (Figure 7). A typical experiment was conducted by heating the rebar steel to attain surface temperatures of 180 °F, 160 °F, 140 °F, or 120 °F. In each experiment once the rebar attained a desirable surface temperature, cement paste with water to cement ratios of 0.4 or 0.5 were prepared and placed over the instrumented rebar. Power supply was then switched off and rebar surface temperature was measured as a function of time. After complete cooling of the rebar to room temperature, temperature measurements were stopped and cement paste was allowed to hydrate and cure.

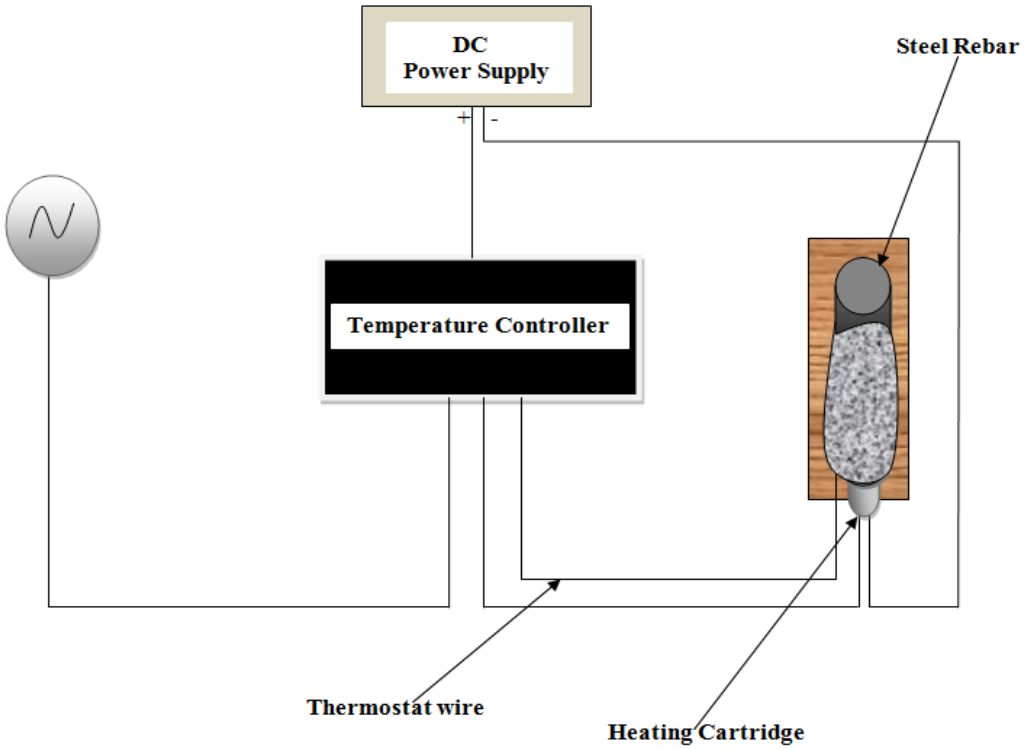

Figure 7. Schematic diagram of experimental apparatus

A set of samples were then prepared and sent for mercury intrusion porosity measurement. Another set of samples were used to perform scanning electron microscopy for qualitative comparison of surface porosity. A third set of samples were used to perform FTIR for water content comparison based on FTIR absorption band at 3450 cm^{-1} wave number that is known to be associated with water content of a given sample.

FTIR Spectroscopy

Theory

Fourier transform infrared (FTIR) spectrophotometry is a measurement technique for collecting infrared spectra to find the phase contents of the sample. Instead of recording the amount of energy absorbed when the frequency of the infra-red light is varied (monochromator), the infra-red light is guided through an interferometer. After passing through the sample, the measured signal is the interferogram. Performing a Fourier transform on this signal data results in a spectrum identical to that from conventional (dispersive) infrared spectroscopy. FTIR spectrometers are cheaper than conventional spectrometers because building an interferometer is easier than the fabrication of a monochromator. In addition, measurement of a single spectrum is faster for the FTIR technique because the information at all frequencies is collected simultaneously. This allows multiple samples to be collected and averaged together resulting in an improvement in sensitivity. Virtually all modern infrared spectrometers are FTIR instruments (Harwood 1989). The results generated through FTIR analysis are referred to as an infrared spectrum. The spectrum graphically illustrates the relative

intensity of the energy absorbed on the *y*-axis versus the frequency of the energy on the *x*-axis. The frequency of the energy can be represented directly in microns (μm) or, more popularly, as reciprocal centimeters (cm^{-1}) referred to as wave numbers. The discrete spectral features present with a FTIR spectrum are known as absorption bands. This technique was used to compare the water content of the cement paste.

Conventional Apparatus

A beam of infrared light is produced and split into two separate beams. One beam is passed through the sample, the other beam passed through a reference which is often the substance the sample is dissolved in. The beams are both reflected back towards a detector (Figure 8); however they first pass through a splitter which quickly alternates which of the two beams enters the detector. The two signals are then compared and a printout is obtained.

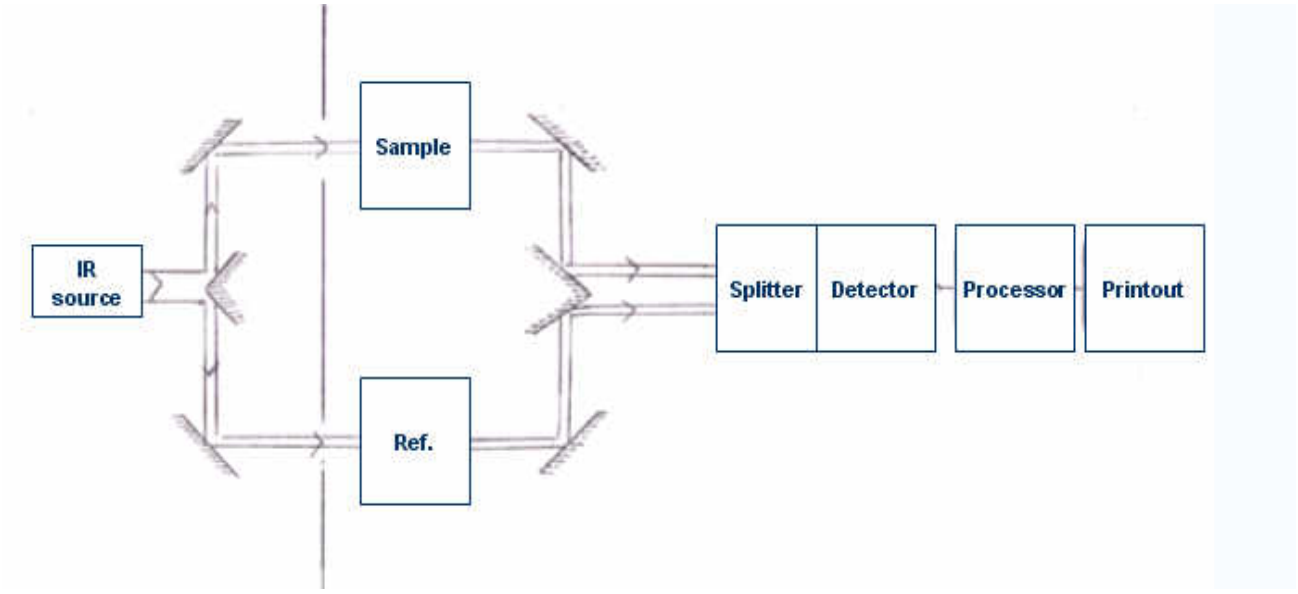

Figure 8. Schematic of FTIR apparatus

Sample Preparation

Solid samples can be prepared in a variety of ways. One common method is to grind a quantity of the sample with a specially purified salt like potassium bromide (KBr) finely to remove scattering effects from large crystals. The KBr used is 100 mg and the sample weight is taken as 2 mg only. This powder mixture is then pressed in a mechanical die press to form a translucent pellet through which the beam of the spectrometer can pass (Harwood 1989). A second technique is the "cast film" technique, which is used mainly for polymeric materials. The sample is first dissolved in a suitable, non hygroscopic solvent. A drop of this solution is deposited on surface of KBr cell. The solution is then evaporated to dryness and the film formed on the cell is analyzed directly. Care is important to ensure that the film is not too thick otherwise light cannot pass through. This technique is suitable for qualitative analysis.

Applications

- Possibly the most important use of FTIR in failure analysis is the identification of the base polymer used to produce the sample. The determination of the composition of the failed component is an essential part of the investigation.
- Fourier transform infrared spectroscopic analysis can provide information regarding the presence of additives and filler materials.
- FTIR is extremely useful in the determination of contaminant materials within the failed part material.
- Fourier transform infrared spectroscopy is a valuable tool in assessing a failed component material for degradation, such as oxidation and hydrolysis.

- The technique is also useful in evaluating the failed sample material for chemical contact. The chemical agent responsible for the cracking may be identified using FTIR.

Mercury Intrusion Porosimetry (MIP)

Theory

The assessment of porosity and pore size distribution of Portland cement used needs to be measured using Mercury intrusion porosimetry (MIP) or density measurement using water impregnation method. MIP is a technique used to measure pore size distribution, and has an advantage in that it is able to span the measurement of pore sizes ranging from a few nanometers, to several hundred micrometers.

As concrete has a distribution of pore sizes ranging from sub-nanometer to many millimeters, MIP has formed an important tool in the characterization of pore size distribution and total volume of porosity. The MIP test carried out is used for quantitative analyses.

Procedure

Mercury is a non-wetting liquid for almost all substances and consequently it has to be forced into the pores of these materials. The MIP technique is widely used because of its ease and simplicity. For cement-based materials the pore size distributions are useful to compare similar systems and to obtain a measure of percolation (A.B. Abell, K.L. Willis and D.A. Lange, 1999). The continuous pore diameter, which is determined from the largest differential intruded volume with respect to diameter, identifies where

percolation has occurred. Pore size and volume quantification are accomplished by submerging the sample under a confined quantity of mercury and then increasing the pressure of the mercury hydraulically. The detection of the free mercury diminution in the penetrometer stem is based on a capacitance system and is equal to that filling the pores. Penetrometer is a glass container with a seal-able lid which is used to hold the sample during testing, sometimes termed a dilatometer. The unit is weighed and calibrated prior to testing to provide known parameters for use in later calculations. The general design is to have an open bulbous body at one end of a long stem into which the specimen is sealed, the unit is then placed into the machine and mercury is introduced via the stem, which remains open, after evacuation. As the applied pressure is increased the radius of the pores which can be filled with mercury decreases and consequently the total amount of mercury intruded increases (Figure 9).

The data obtained give the pore volume distribution directly and with the aid of a pore physical model, permit a simple calculation of the dimensional distribution of the pore size. Determination of the pore size by mercury penetration is based on the behavior of non-wetting liquids in capillaries. A liquid cannot spontaneously enter a small pore which has a wetting angle of more than 90 degrees because of the surface tension (capillary depression); however this resistance may be overcome by exerting a certain external pressure. The pressure required is a function of the pore size, the relationship between pore sizes exerted when the pore is considered to be cylindrical, is expressed as:

$$pr = 2\sigma \cos(\theta) \ldots\ldots\ldots\ldots (1)$$

Where: r = pore radius.

σ = surface tension of mercury.

θ = contact angle (wetting angle).

p = absolute pressure exerted.

The relationship is commonly known as the Washburn equation (E.W. Washburn, 1921). Although in almost any porous substance there are no cylindrical pores, this equation is generally used to calculate a pore size distribution from mercury porosimetry data. The Washburn equation is derived from the following considerations: in a capillary with a circular section, the surface tension of the liquid is exerted in the area of contact over a length equal to the pore circumference. This force, $2pr\theta$, is perpendicular to the plane of the contact surface. The force tending to push the liquid out of the capillary is:

$$2\ p\ r\ \sigma\ \cos\theta \ldots. (2)$$

Against this force, the external pressure will be exerted over the area within the contact circumference, equal to:

$$pr^2p=?... (3)$$

When equilibrium is reached, these two forces have the same value:

$$2\ p\ r\ \sigma\ \cos\theta = pr^2p\ldots.. (4)$$

Equation (1) therefore shows the pore radius is inversely proportional to the pressure:

$$r = 2\sigma\ \cos\theta / p\ldots\ldots (5)$$

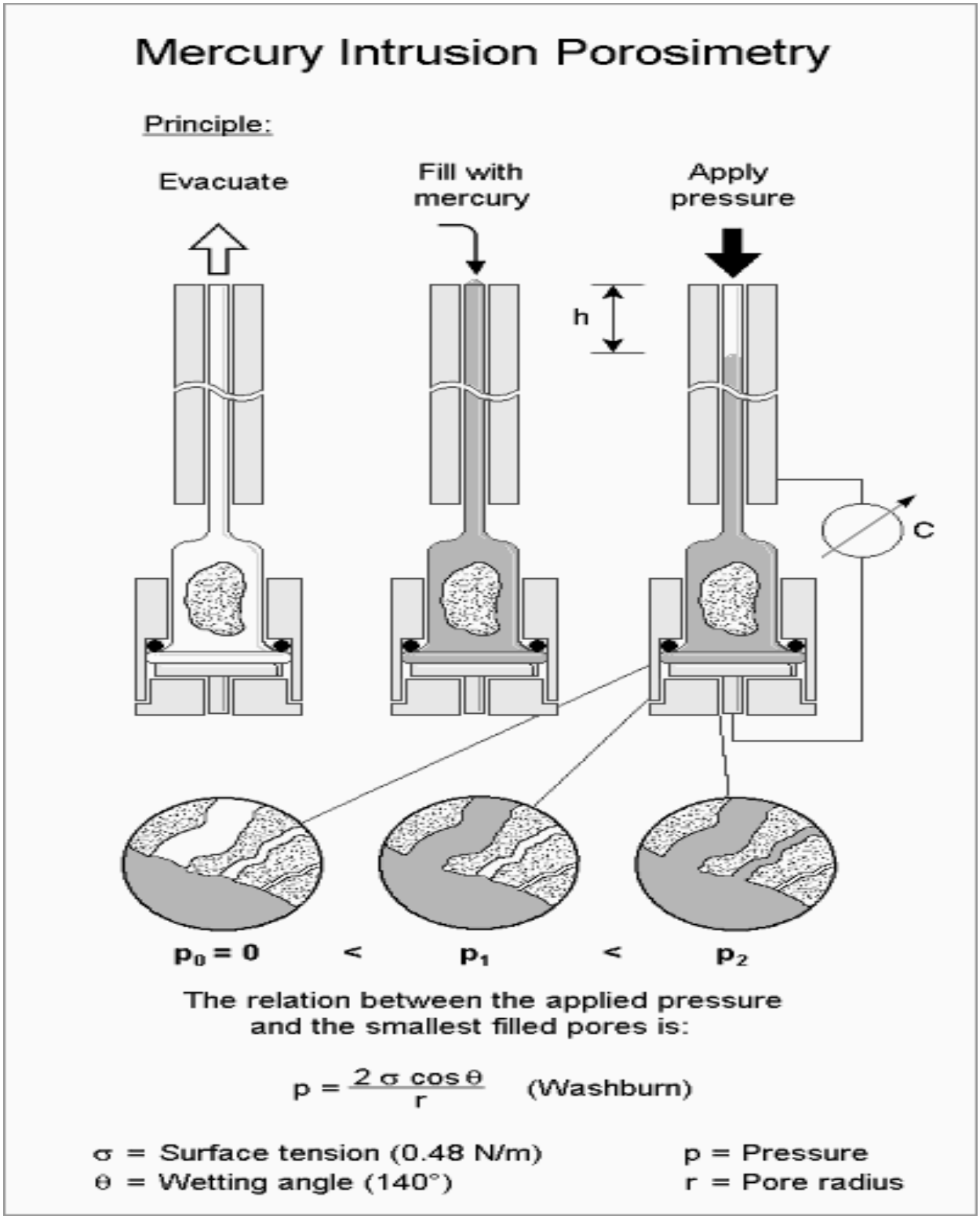

Figure 9. MIP apparatus and procedure. Courtesy Fraunhofer Institute for Building Physics.

When using mercury (taking the surface tension as 480 mN/m^2 and wetting angle as 141.3°) and assuming that all pores are cylindrical, the following relationship is obtained.

$$r = 7500/p \quad \text{..... (6)}$$

Where r is the pore radius in nm

p is absolute applied pressure in kg/sq.cm

For irregular shaped pores the ratio between the pore cross-section (related to the pressure exerted) and the pore circumference (related to the surface tension) is not proportional to the radius and depending on the pore shape, equation (5) will give lower values. The wetting angle (taken as 141.3°) depends on the nature of the sample, and should therefore be considered as an average value only. Surface tension should also be considered as a variable value. At 25 °C it is 484.2 dynes/cm^2, while at 50 °C it is 472 dynes/cm^2; 480 dynes/cm^2 has been taken as an average value.

Specimens prepared for testing are dried to remove all moisture from the pore structure. They are then placed into sealed 'penetrometers' which are weighed both before and after being loaded with the specimen. The penetrometers are placed into the machine where they are evacuated and then filled with mercury.

The pressurized testing then commences and the machine calculates and records how much mercury is being forced into the pore structure based on the above equations.

The results obtained from the instrument are:-

i. pore size distribution (macro range of porosity spectrum)

ii. hysteresis curve

iii. specific surface

iv. bulk density

v. total porosity (%)

vi. particle size distribution

Normally these data are transferred into a spreadsheet or similar application for further detailed analysis.

Scanning Electron Microscope Analysis

Theory

The scanning electron microscope is one of the most versatile instruments for investigating the microstructure of materials. Under electron bombardment, a variety of different signals is generated that can be used for materials characterization. Using secondary electrons (produced as a result of interactions between the beam electrons and weakly bound conduction electrons of sample atoms), scanning electron microscopy (SEM, Figure 10) expands the resolution range to a few nanometers (under favorable conditions), thus bridging the gap between optical microscopy and transmission electron microscopy. In addition to the higher lateral resolution, SEM also has a much greater depth of field compared to optical microscopy, due to the small size of the final lens aperture and the small working distance. Scanning electron microscopy offers

possibilities for micrograph formation that are usually easy to interpret and will reveal clear pictures of as-polished and etched cross sections as well as rough surfaces and particles. Energy-dispersive x-ray microanalysis using equipment routinely attached to the scanning electron microscope features qualitative and quantitative analysis of the chemical composition with a typical lateral resolution of a micrometer and a typical depth resolution of a few tenths of a micrometer. Due to the relatively easy handling, SEM has found a wide range of applications in materials research, materials development, failure analysis, and quality control. The main components of the scanning electron microscope include the electron gun, probe-forming column (consisting of magnetic electron lenses, apertures, and scanning coils), electron detectors, and vacuum system (ASM Handbook Failure Analysis Volume 11).

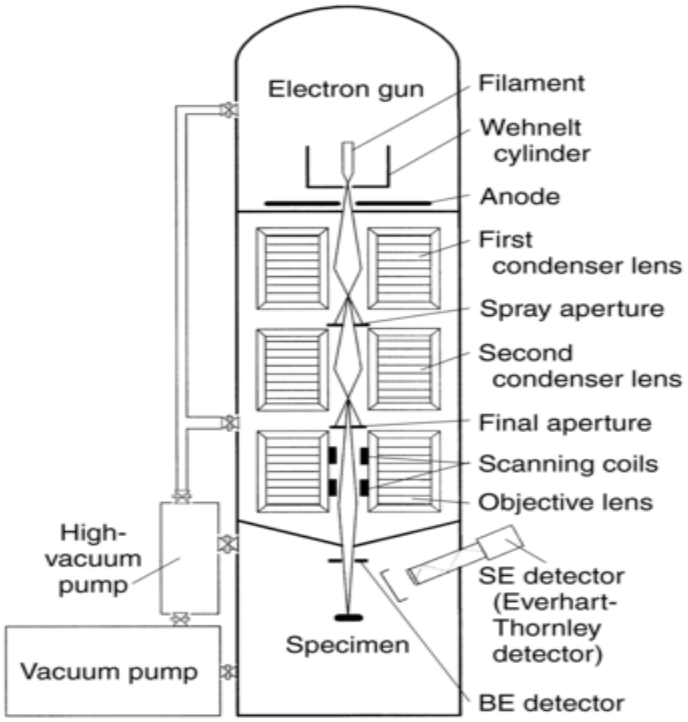

Figure 10. Schematic diagram of SEM apparatus (ASM Handbook Failure Analysis Volume 11).

The SEM micrographs were used for analysis purpose to observe morphology of the concrete and cement samples with different rebar temperatures and water to cement ratios and relate amount of surface porosity at rebar-concrete interface. It was used to examine the morphological characteristics and the nature of porosity at the rebar-concrete interface. The microscope used in the investigation was a JEOL 840 with W-filament electron gun. The system has an Energy Dispersive Spectroscope (EDS) that was used for elemental analysis of the cement samples.

Sample Preparation

All samples were coated with a thin layer of gold using a Cressington 108 Sputter Coater before SEM analysis is performed to provide enough conductivity to prevent sample charging while the analysis would take place. The coating process is done for an approximate time of two minutes after which the sample was removed from the coating chamber. The sample will not charge now when analyzed under the SEM.

CHAPTER 4

RESULTS AND DISCUSSIONS

Cast Samples

Investigation on the effect of w/c ratios (0.40, 0.45, and 0.50), rebar temperature (77 ^{o}F and 150 ^{o}F) determines their influence of these parameters on rebar-concrete bond strength. The effect of the addition of fly ash on bond strength was analyzed by comparing results for control specimens with fly ash containing ones. The failure mode experienced during the pullout process was the fracture as shown in Figure 11. Failure occurred along the length of the rebar.

Figure 11. Pullout failure mode

The tensile tester applied a monotonic load on the rebar embedded in the concrete until bond slip/failure occurred. The pullout load versus slippage readings were collected electronically and recorded by the computer. The pullout rate used was 0.08 in/min with data recorded every one second. The pullout experiment was carried out for 3 specimens per run for the fly ash samples and the values for pullout force when the fracture takes place in the samples was recorded, which are shown in Tables 6 and 7. The fractured concrete samples were then labeled and preserved properly to be used for further analysis.

Table 6. Measured bond strength magnitudes for fly ash added concrete mix at different w/c ratios and rebar temperatures for 10 days, 8-in embedment.

FLY ASH MIXED CONCRETE 10 DAY PULLOUT TEST RESULTS						
w/c ratio	**0.4**		**0.45**		**0.5**	
Temperature (^{o}F)	*77*	*150*	*77*	*150*	*77*	*150*
Pullout Force(lbf)	7101	9928*	5850	4666	3364	4875
	8078	5071	2909	2458	3321	1603
	6540	5170	3852	4529	3412	1102
	4011	4070	3071	5699*	3365	1259
	4325	6881	4891	5114	2201	4046
	7737	5114	5815	4185	2248	343*
	4886	2259*	3372	4897	2849	2426
	4322	4757	4886	4666	2389	594*
	4472	7541	2267*	NA	3327	NA

Table 7. Measured bond strength magnitudes for fly ash added concrete mix at different w/c ratios and rebar temperatures for 28 days, 8-in embedment.

FLY ASH MIXED CONCRETE 28 DAYS PULLOUT TEST RESULTS						
w/c ratio	**0.4**		**0.45**		**0.5**	
Temperature (^{o}F)	*77*	*150*	*77*	*150*	*77*	*150*
Pullout Force(lbf)	9200	6413	6768	11470*	5936	6850
	8100	5162	8260	3523	4038	6666
	8800	7694	8056	5715	7195	5944
	12400	17440*	9479	8865	10460	6314
	13998	4260	8424	5361	4102	6169
	11690	7772	6880	6285	3101*	5463
	10800	12560*	6615	6121	8456	6207
	10220	9420	9372	11320*	13800*	6660
	NA	8545	6789	8220	3238*	5868

The average shear stress of the bond was calculated using the maximum shear stress equation (Abdolkarim, 2005).

$$\mu_{max} = P_{max} / л2rl_b \text{.....(7)}$$

Where P_{max} is the bond force, $2r$ is the rebar diameter; l_b is the embedded bond length.

There are unusually high or low pullout force outliers (*) in the pullout experimental data that was recorded, and these values were not used for the calculation of the average pullout force and the standard deviation as there was too large a deviation based on the average values. These may be caused due to some experimental errors.

The average pullout strength along with the calculated shear stress results for fly ash containing mix concrete specimens cast at 77 ^{o}F and 150 ^{o}F for the 10-day and 28 days are shown Table 8.

Table 8. Calculated average bond strength and shear strength magnitudes for fly ash added concrete mix at different w/c ratios and rebar temperatures, 8-in embedment.

w/c	Temp (^{o}F)	Pullout Force (lbf)		Shear Stress (psi)	
		10 day	28 day	10 day	28 day
0.40	77	5719(±1631)	10651(±1985)	303	565
0.45		4330(±1189)	7849(±1133)	230	416
0.50		2942(±526)	6697(±2525)	156	355
0.40	150	5514(±1232)	7038(±1850)	293	373
0.45		4359(±887)	6299(±1790)	231	334
0.50		2551(±1569)	6238(±443)	135	331

The standard deviation is high as concrete is a composite material and it contains aggregates of different size and nature. These aggregates are non uniformly distributed in the vicinity of rebar-concrete bonding which affect the pullout force that is applied in the experiment.

The pullout experiment was carried out at 9 specimens per run for the non fly ash samples and the values for pullout force when the fracture takes place in the samples was recorded, which are shown in Tables 9 and 10. The fractured concrete samples were then labeled and preserved properly to be used for further analysis.

Table 9. Measured bond strength magnitudes for non fly ash concrete mix at different w/c ratios and rebar temperatures for 10 days, 8-in embedment.

NON FLY ASH MIXED CONCRETE (CONTROLED) 10 DAYS PULLOUT TEST RESULTS						
w/c ratio	**0.4**		**0.45**		**0.5**	
Temperature (^{o}F)	*77*	*150*	*77*	*150*	*77*	*150*
Pullout Force(lbf)	1480*	3662	5882	1730	3930	3254
	3634	4483	4051	7023*	4534	2343
	7705	2977	5235	3132	3666	3326
	5179	2772	4795	4191	5189	1791
	5251	8024	3480	3202	4617	2300
	1872*	1992*	3341	2488	3812	1663
	4513	3987	3293	6746*	2090	3981
	4494	7286	4964	2728	4464	3979
	5315	4102	4191	7659*	4255	NA

Table 10. Measured bond strength magnitudes for non fly ash concrete mix at different w/c ratios and rebar temperatures for 28 days, 8-in embedment.

NON FLY ASH MIXED CONCRETE (CONTROL) 28 DAYS PULLOUT TEST RESULTS						
w/c ratio	**0.4**		**0.45**		**0.5**	
Temperature (^{o}F)	*77*	*150*	*77*	*150*	*77*	*150*
Pullout Force(lbf)	5930	11370*	5320	3903	6687	5877
	6770	4153	4964	5992	5297	6408
	9530*	6016	5034	5146	1758*	3400
	7283	5007	6295	5340	7243	5283
	6174	4427	9756	4870	6609	5380
	5630	2926*	4720	4123	6282	3860
	6408	6268	5490	5909	4287	6346
	5136	3727	5624	7817*	3345	4977
	4416	6411	4658	5450	5170	3470

The pullout strength results for non-fly ash mix concrete specimens cast at 77 ^{o}F and 150 ^{o}F for the 10-day and 28 days are shown in Table 11.

Table 11. Measured bond strength magnitudes for non fly ash concrete mix at different w/c ratios and rebar temperatures, 8-in embedment.

w/c	Temp (^{o}F)	Pullout Force (lbf)		Shear Stress (psi)	
		10 day	28 day	10 day	28 day
0.40	77	5155(±1272)	5968(±912)	273	317
0.45		4359(±916)	5762(±1581)	231	306
0.50		4062(±875)	5615(±1334)	215	298
0.40	150	4661(±1942)	5144(±1092)	247	273
0.45		2911(±822)	5092(±763)	154	270
0.50		2829(±928)	5000(±1172)	150	265

Graphical representation of the data for fly ash mix concrete and the control experiments showing the trends on the influence of the temperature and different water/cement ratios are shown in Figures 12 & 13 for the fly ash containing mix and control experiments respectively. Shear stress value increases as the water-cement ratio decreases. This is shown for both 77 ^{o}F and 150 ^{o}F samples.

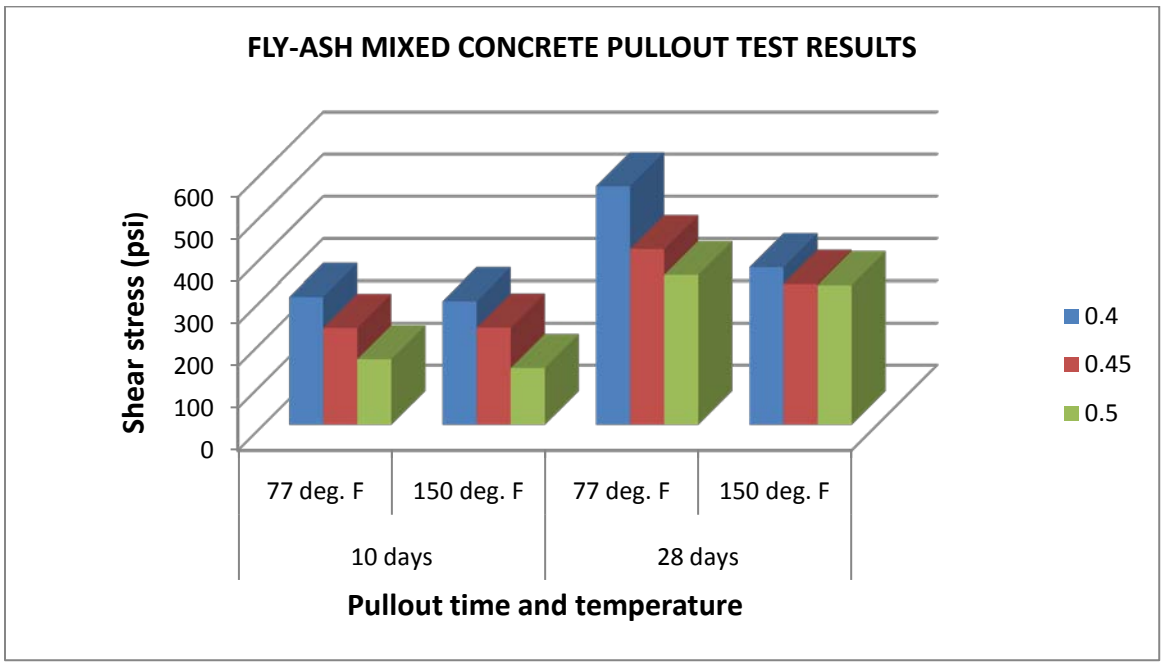

Figure 12.Fly ash mixed concrete pullout test results

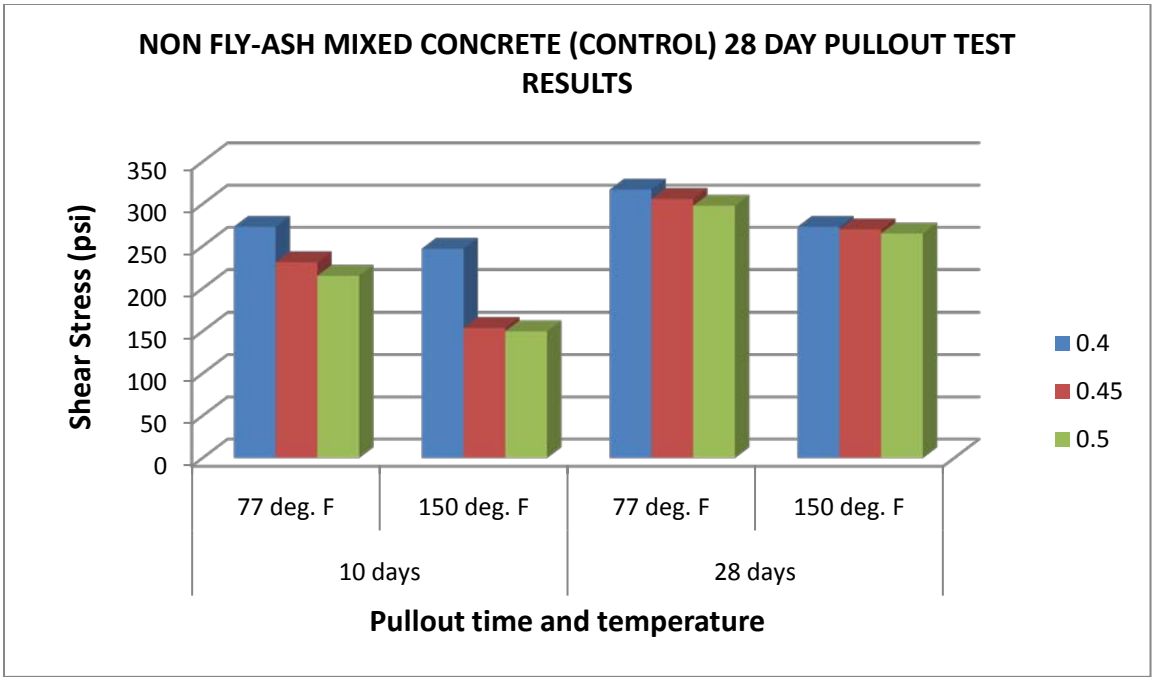

Figure 13.Non-fly ash mixed concrete pullout test results

The primary objective of this study was to identify the effect of rebar temperature at the concrete pouring stage on the concrete- rebar bond strength, the effect of changing the water to cement ratio, using fly ash on the concrete mix versus non-fly ash on the concrete mix. Curing is one of the most important steps in concrete construction, because proper curing greatly increases concrete strength and durability. Concrete hardens as a result of hydration: the chemical reaction between cement and water. However, hydration occurs only if water is available and if the concrete's temperature stays within a suitable range. During the curing period-from five to seven days after placement for conventional concrete-the concrete surface needs to be kept moist to permit the hydration process. The experimental results can be categorized into rebar temperature, water to cement ratio, and fly ash on the concrete mix versus non-fly ash on the concrete mix effects. These parameters allowed for the examination determination of the concrete-rebar bond

strength. The 28 days data show a better trend with a smaller pullout force deviations than the 10 days data. Large pullout force deviations for 10 day samples are due to incomplete concrete hydration. The results of the experimental investigation can be summarized as follows:

1. The 28 days data shows higher strength than the 10 days data as the hydration process is considered to be complete for the 28 days samples whereas it is incomplete for the 10 days samples.
2. The bond strength was significantly influenced by the water to cement ratio. The 28 day shear stress measurements showed that the lower the water to cement ratio the higher the rebar concrete bond strength.
3. The w/c ratio of 0.4 gives higher strength when compared to w/c ratio of 0.5 as too much water will result in settling and segregation of the sand/aggregate components.
4. Based on the 10 days and 28 days data, there is a reduction in the peak pullout load as the temperature increased from 77 ^{o}F to 150 ^{o}F for both the fly ash concrete mix and non-fly concrete mix experiments.
5. There is an increase in shear strength (after 28 days of hydration) due to addition of fly ash when samples were prepared at 77 ^{o}F with 78%, 36% and 19% for w/c ratios of 0.4, 0.45 and 0.5 respectively. Also there is an increase of shear strength due to addition of fly ash for samples prepared at 150 ^{o}F with 37%, 24% and 25% for w/c ratios of 0.4, 0.45 and 0.5.

Heated Rebar Results

Figure 14 shows comparison of cooling curves for all four initial temperatures for water-cement ratio of 0.5 for which values were recorded experimentally and the graphs were plotted. The approximate time taken to reach the room temperature of 77 ^{o}F was almost 50 minutes.

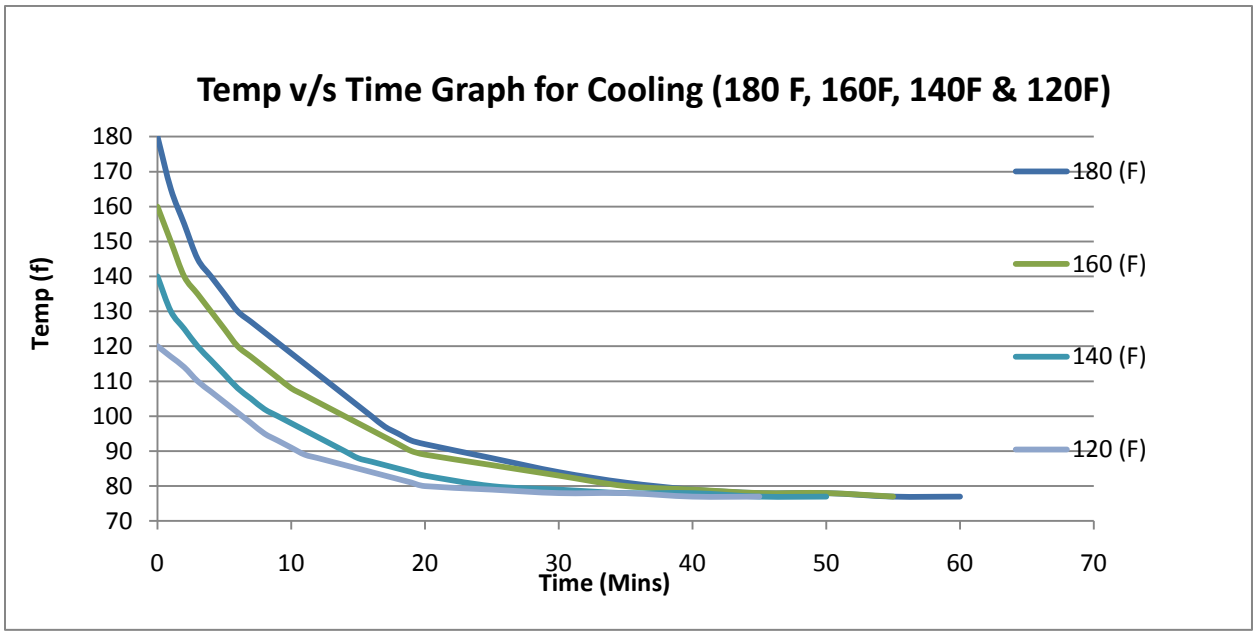

Figure 14. Comparison of cooling curves for rebar temperatures vs time plots for different initial rebar temperatures (w/c = 0.5).

The graph of rebar temperature vs time curve for rebars heated at different temperatures with water-to-cement ratio of 0.4 is shown in Figure 15.

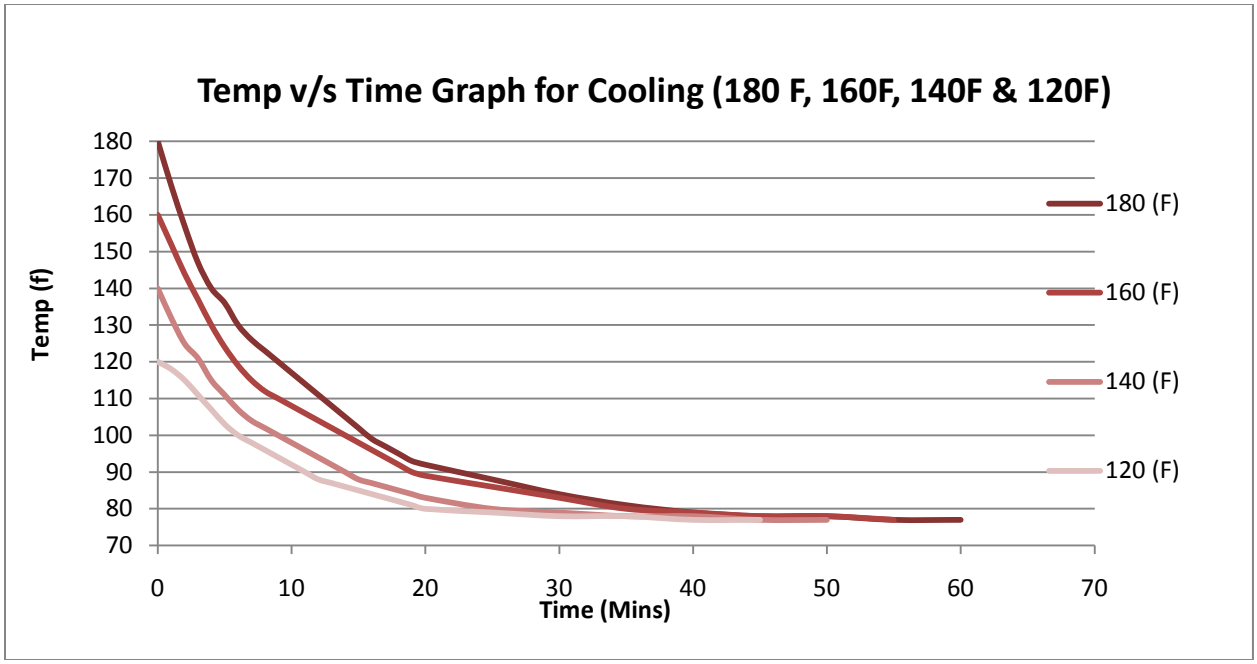

Figure 15.Comparison of cooling curves for rebar temperatures vs time plots for different initial rebar temperatures (w/c = 0.4).

The slope of rebar temperature vs. time curve shows higher the temperature of the steel rebar, faster is the drying process at the rebar-concrete interface. This results in formation of pores at the rebar-concrete interface. There is no significant difference between the graphs of water to cement ratios of 0.5 and 0.4.

It is expected that the higher the temperature gradient between the heated rebar and the neighboring cement at the rebar-concrete interface, the faster drying of the interface and lower the hydration of the interface (Equation 8). Poor hydration not only produces lower strength concrete at the rebar-concrete interface but also weaker cement to rebar bonding. Since the hydration of cement is a chemical process, a high ambient temperature will increase the rate at which the concrete hydrates. High solar radiation during construction also plays an important role in increasing the concrete temperature and the rate of hydration. We also know that dry shrinkage takes place at low w/c ratio.

The w/c ratios were chosen to provide a wide strength rate as used in the construction of Portland cement concrete (PCC) pavements. The w/c ratio chosen for the construction purpose is optimized to achieve the required strength, durability and permeability requirements.

Figure 16 shows the directions of heat flow from rebar toward the bulk cement and moisture transfer toward the heated rebar (direction of negative moisture gradient). The more the water contents at the interface and higher the temperature the more is the porosity percentage. Figure 17 shows a schematic of the expected heat affected cement indicating higher pore density and larger pore size distribution at the rebar-concrete interface for higher w/c ratios and higher rebar temperatures.

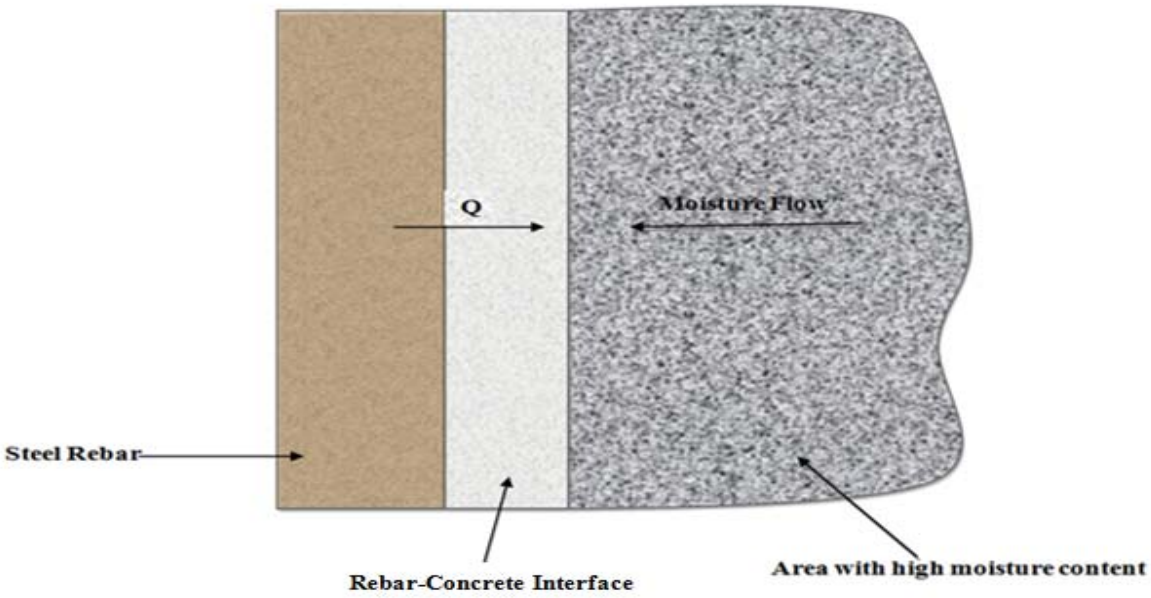

Figure 16.The schematic diagram of rebar-concrete interface showing conduction of heat from heated rebar toward the surface and moisture transfer toward the heated rebar

$$\dot{Q} = kA\left(\frac{\Delta T}{\Delta X}\right) \text{.....(8)}$$

where $\dot{Q}$ is heat transfer rate, k is thermal conductivity of cement, A is the heat transfer surface area and $\frac{\Delta T}{\Delta X}$ is the temperature gradient. For a fixed ΔT, higher is the $\dot{Q}$, drier is the rebar-concrete interface.

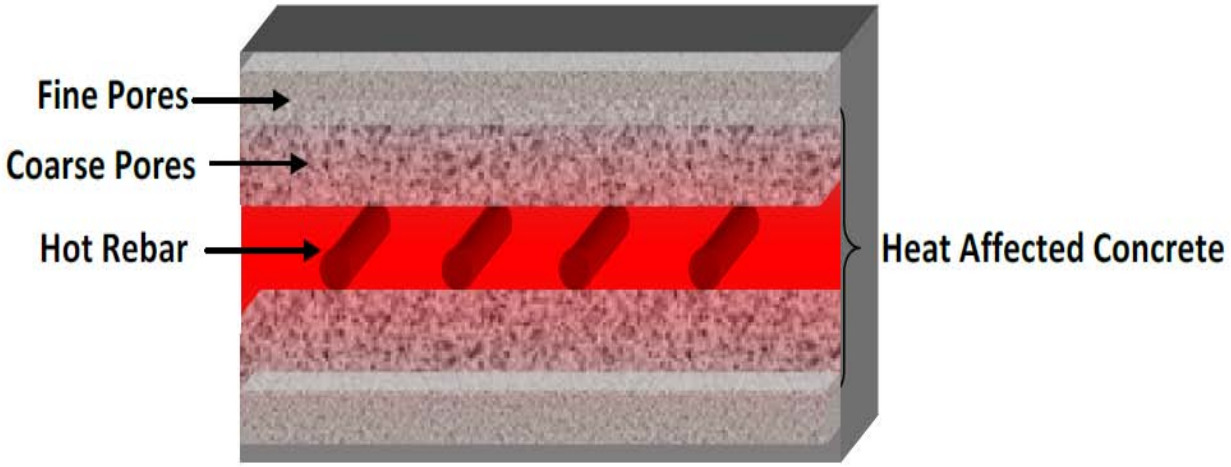

Figure 17. Heat affected concrete around the hot steel rebar

FTIR Spectroscopy

The FTIR experiment was performed on all the samples but in batches of two- 0.4 w/c and 0.5 w/c. First the FTIR was performed on the 0.5 w/c samples (Figure 18). The water absorption band is shown clearly for all the samples at wavenumber 3450(cm^{-1}). The absorbance band intensity for 120 ^{o}F sample is the highest followed by 140 ^{o}F sample, 160 ^{o}F sample and 180 ^{o}F sample.

The FTIR was then performed on the 0.4 w/c samples (Figure 19). The water absorption band is shown clearly for all the samples again at wavenumber 3450(cm^{-1}). The absorbance band for 120 ^{o}F sample is the highest followed by 140 ^{o}F sample, 160 ^{o}F sample and 180^{o}F sample.

The spectrum graphs below show that irrespective of the water-cement ratio used for preparation of the samples, the moisture content at the rebar-concrete interface is higher for the 120 ^{o}F sample and it is the lowest for 180 ^{o}F sample. This leads to higher porosity for the 180 ^{o}F sample at the rebar-concrete interface as compared to the other three samples. A quantative analysis of pore density and pore size distribution is done using MIP and the results are presented in the following sections.

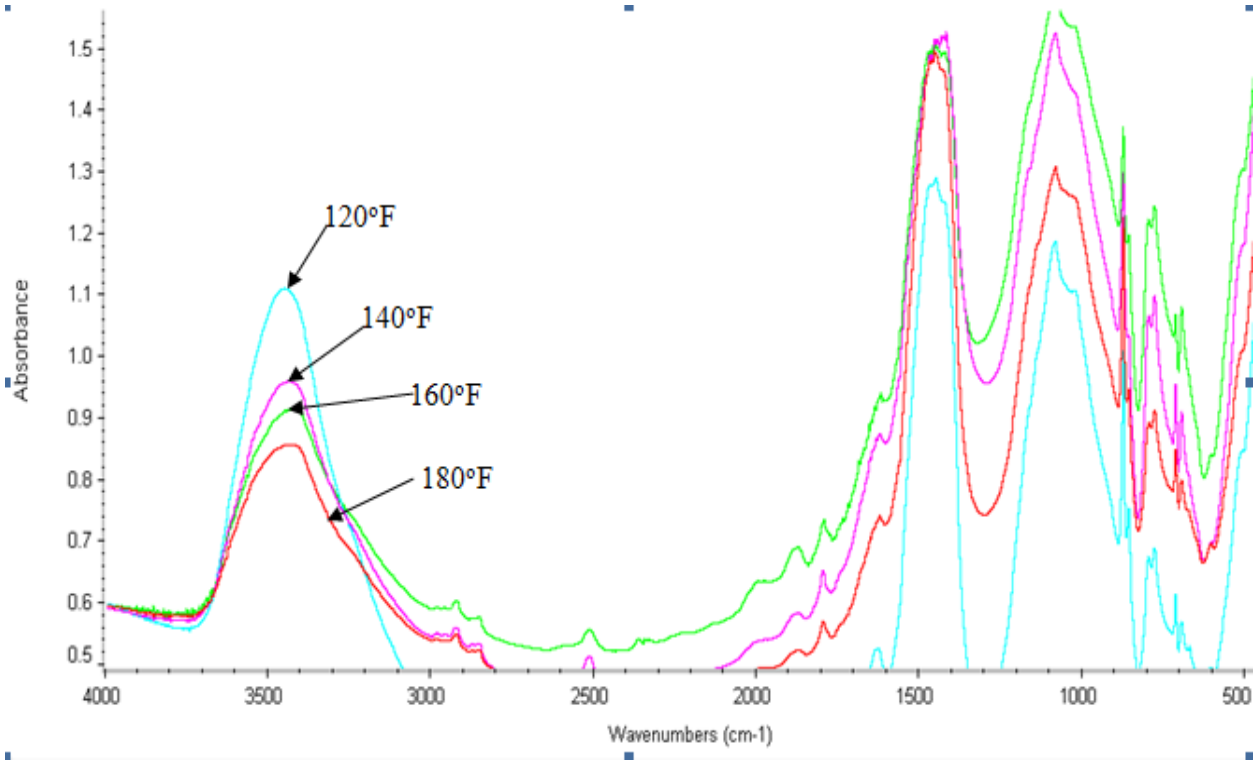

Figure 18. FTIR spectra for 0.5 w/c samples

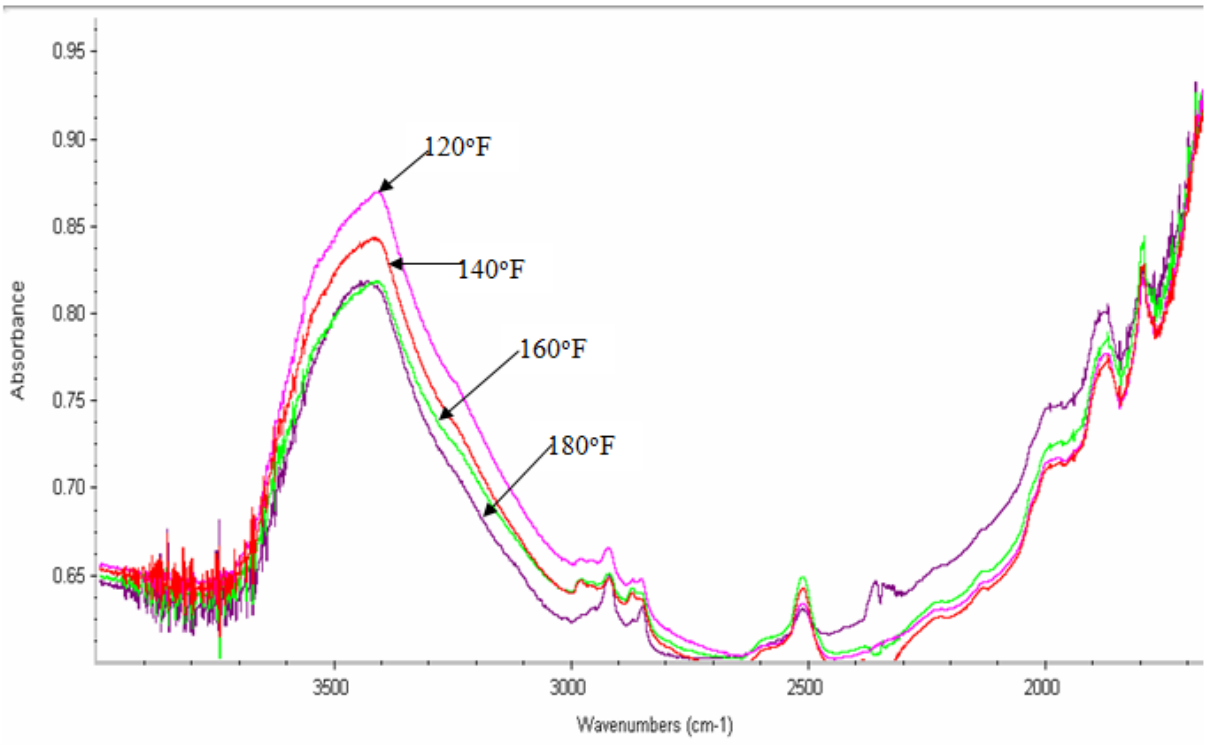

Figure 19. FTIR spectra for 0.4 w/c samples

Mercury Intrusion Porosimetry (MIP)

The above mentioned discussion in the heated rebar experiment regarding the poor hydration at the rebar-concrete interface can be shown with the help of quantitative analysis such as the MIP. The 0.4 w/c ratio samples were sent for the MIP test characterized as follows:

Anol_A → 180 ^{o}F

Anol_B → 160 ^{o}F

Anol_C → 140 ^{o}F

Anol_D → 120 ^{o}F

Only one batch of these samples was sent for the MIP test, hence the data obtained is limited. The samples were sent to Texas Transportation Institute at Texas A&M University, College Station for the MIP tests. The MIP results were recorded graphically for all the samples. The MIP overlays for all the samples (Figure 20 top curve) shows the highest percent mercury intrusion porosity values for the sample prepared at 160^{o}F which is followed by those for 180 ^{o}F, 140 ^{o}F and 120 ^{o}F samples as a function of pore diameter. The area under the curve for all the samples shows the amount of porosity in the rebar-concrete vicinity. The total area under the curve for the 120 ^{o}F sample is the least as compared to the other three samples. This goes to prove that the porosity volume for this sample is also the least which goes with the trend that lower the temperature of the rebar, lower is the porosity at the rebar-concrete interface. The Normalized volume vs. the pore size diameter for individual samples was also plotted (Figures 21 for 180 ^{o}F, Figure 22 for 160 ^{o}F, Figure 23 for 140 ^{o}F, and Figure 24 for 120 ^{o}F). These plots showed that the pore diameter distribution shifted to higher pore diameter range with an increase in rebar temperature.

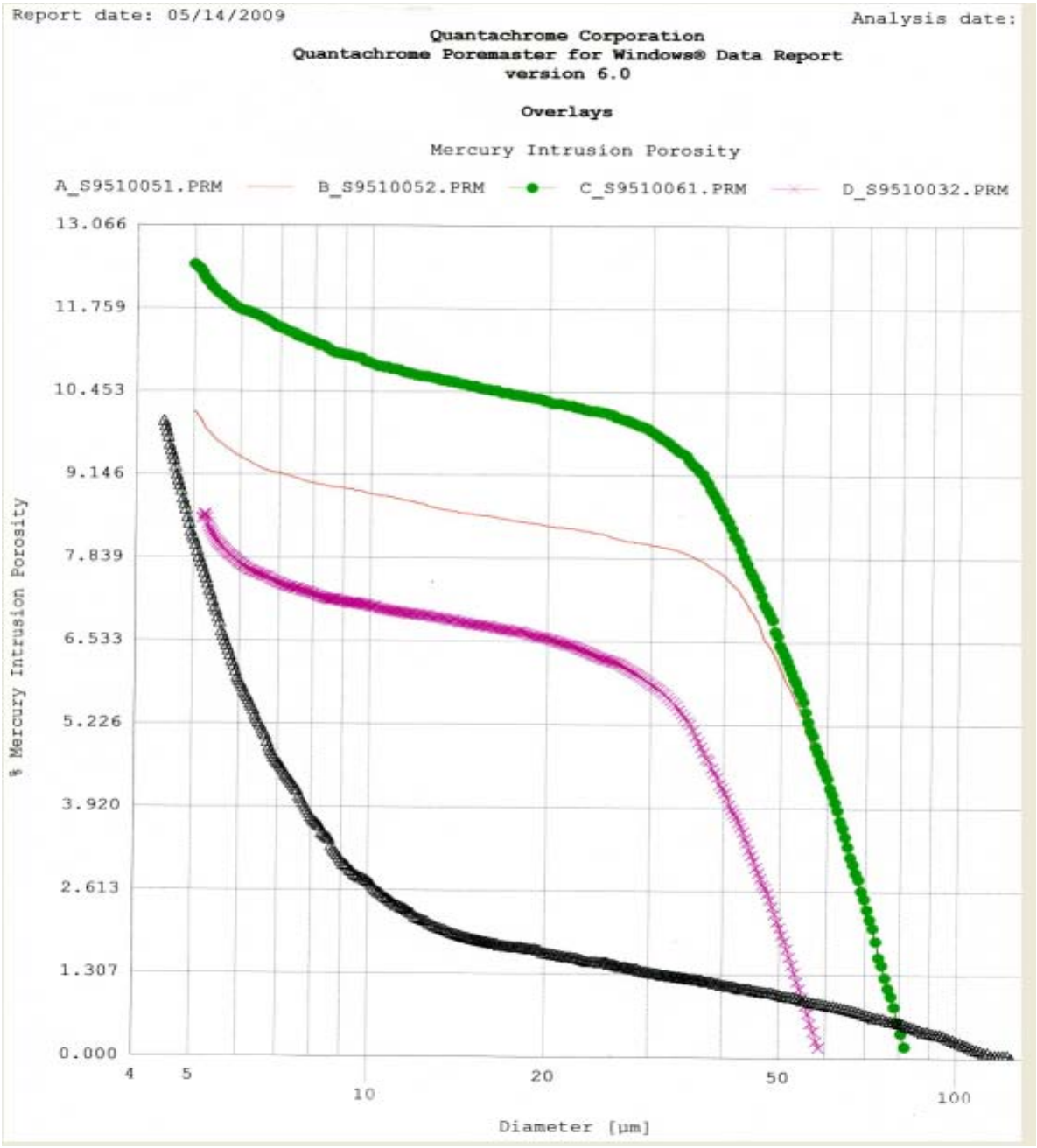

Figure 20. Mercury intrusion porosity overlays

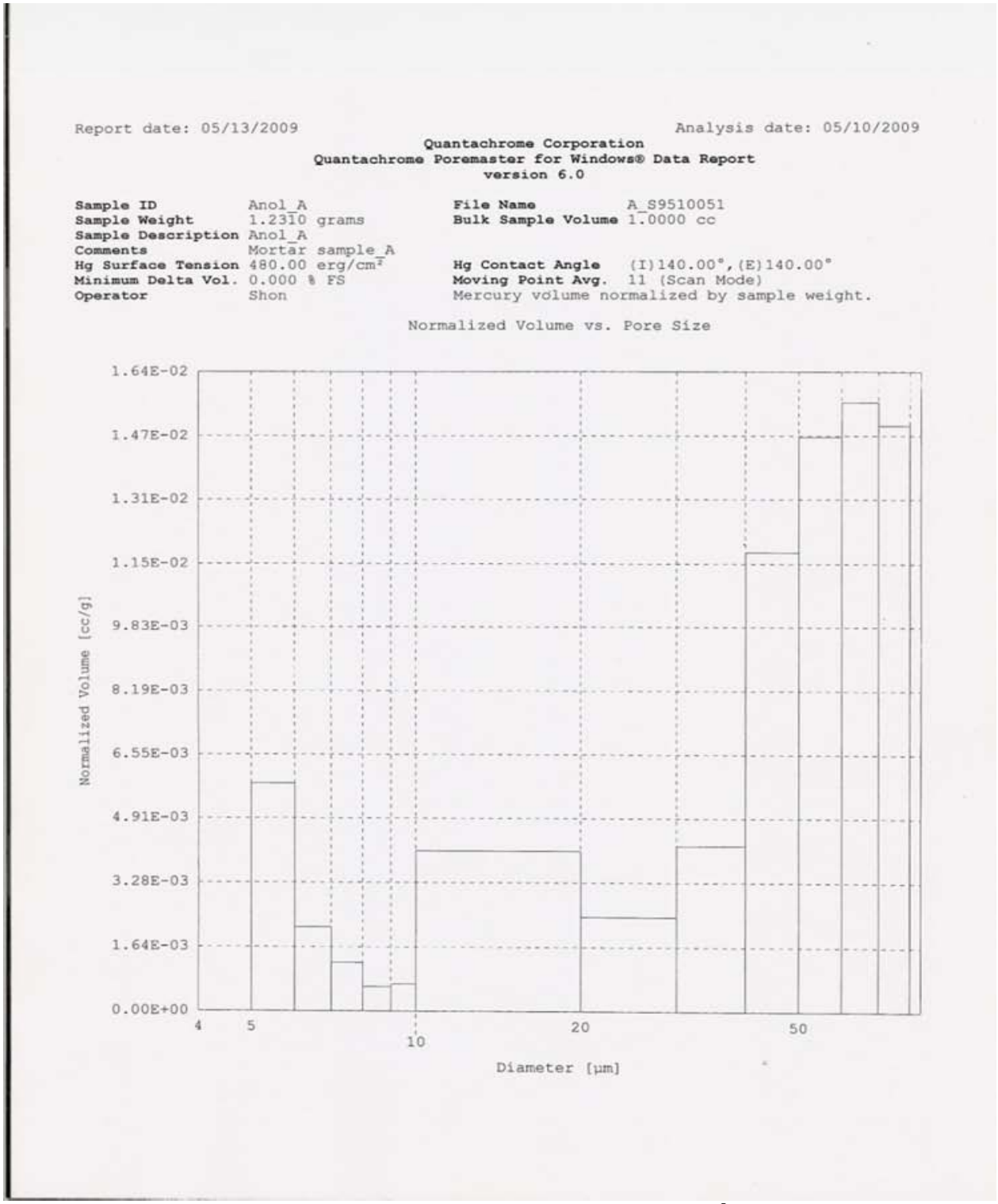

Figure 21. Normalized volume vs. pore size diameter for 180 ^{o}F sample

Report date: 05/13/2009 Analysis date: 05/10/2009

Quantachrome Corporation
Quantachrome Poremaster for Windows® Data Report
version 6.0

Sample ID	Anol_B	**File Name**	B_S9510052
Sample Weight	1.1173 grams	**Bulk Sample Volume**	1.0000 cc
Sample Description	Anol_B		
Comments	Mortar sample_B		
Hg Surface Tension	480.00 erg/cm²	**Hg Contact Angle**	(I)140.00°,(E)140.00°
Minimum Delta Vol.	0.000 % FS	**Moving Point Avg.**	11 (Scan Mode)
Operator	Shon	Mercury volume normalized by sample weight.	

Normalized Volume vs. Pore Size

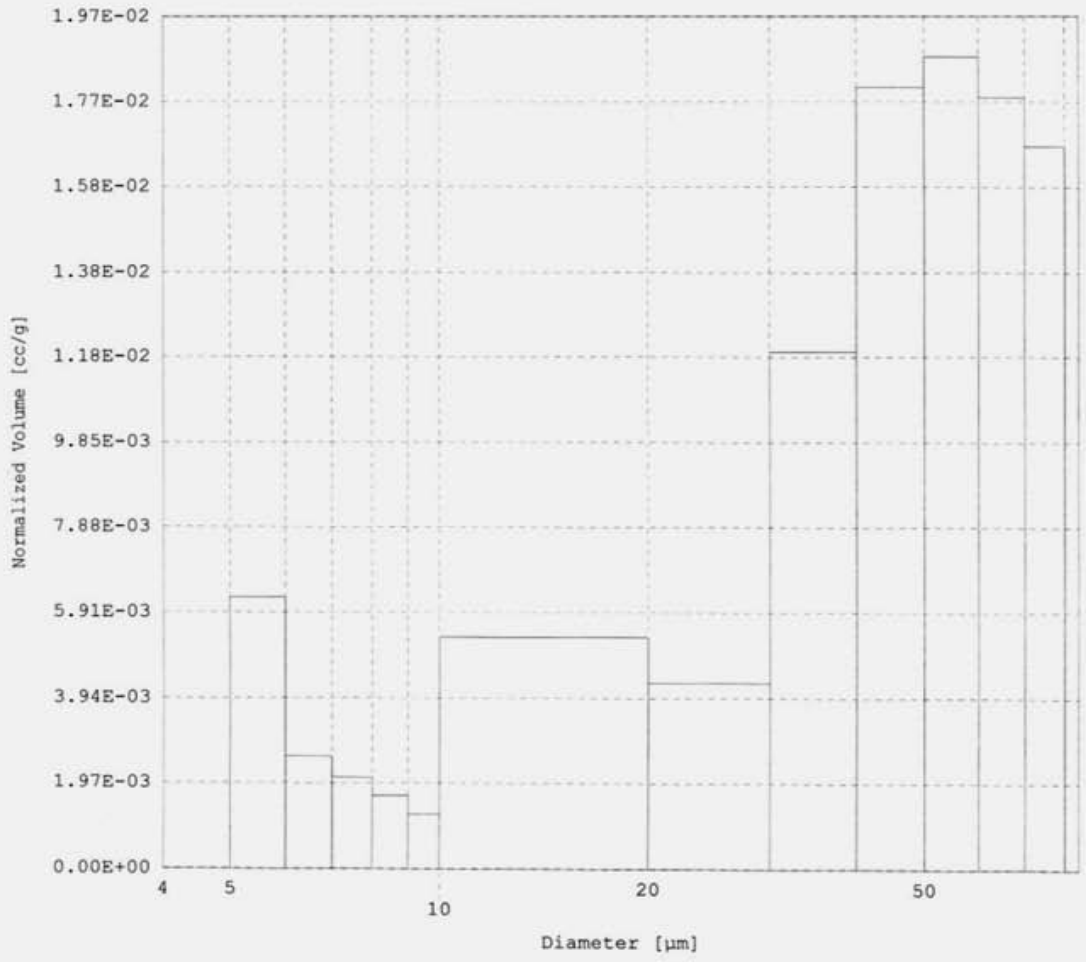

Figure 22. Normalized volume vs. pore size diameter for 160 ^{o}F sample

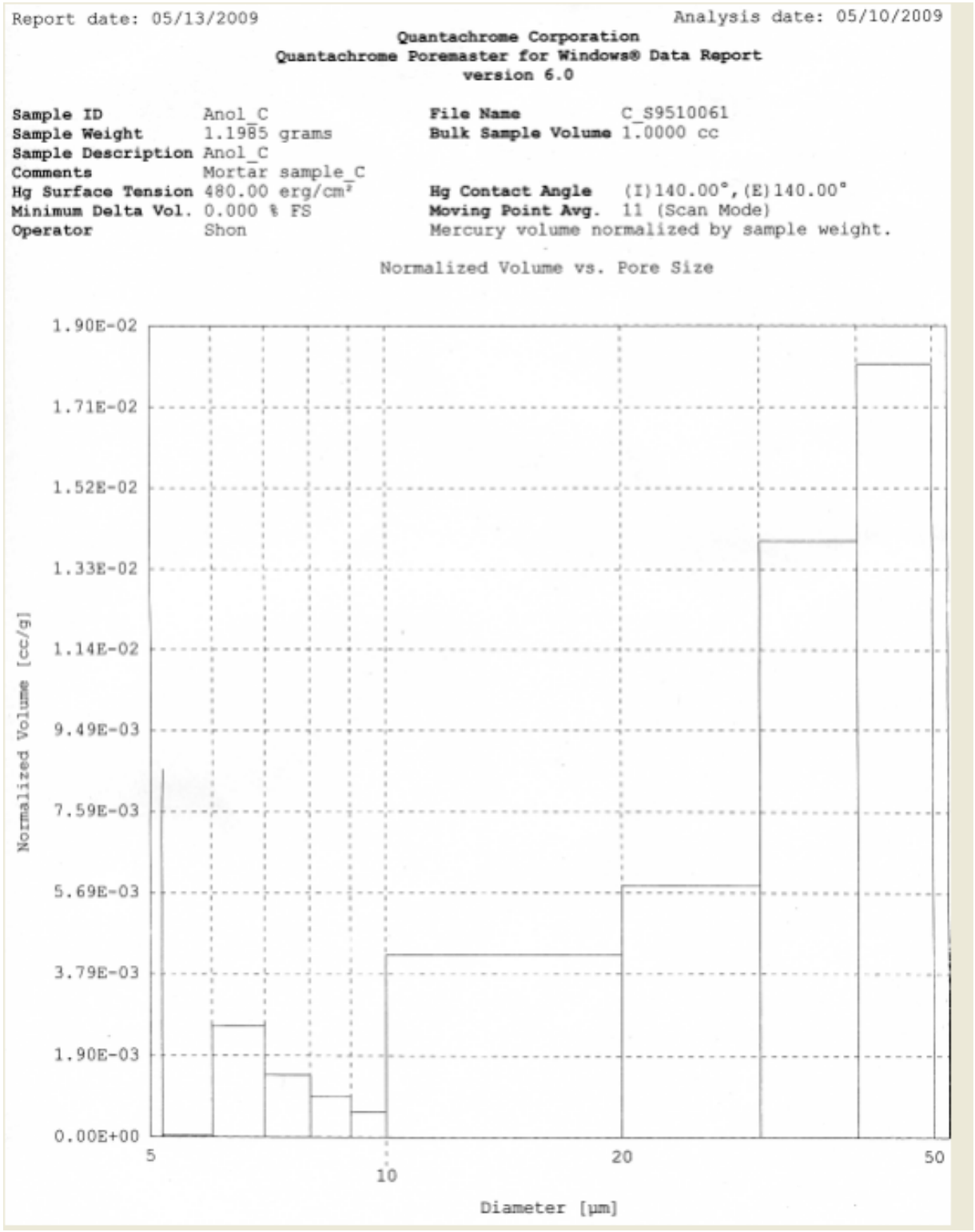

Figure 23. Normalized volume vs. pore size diameter for 140 ^{o}F sample

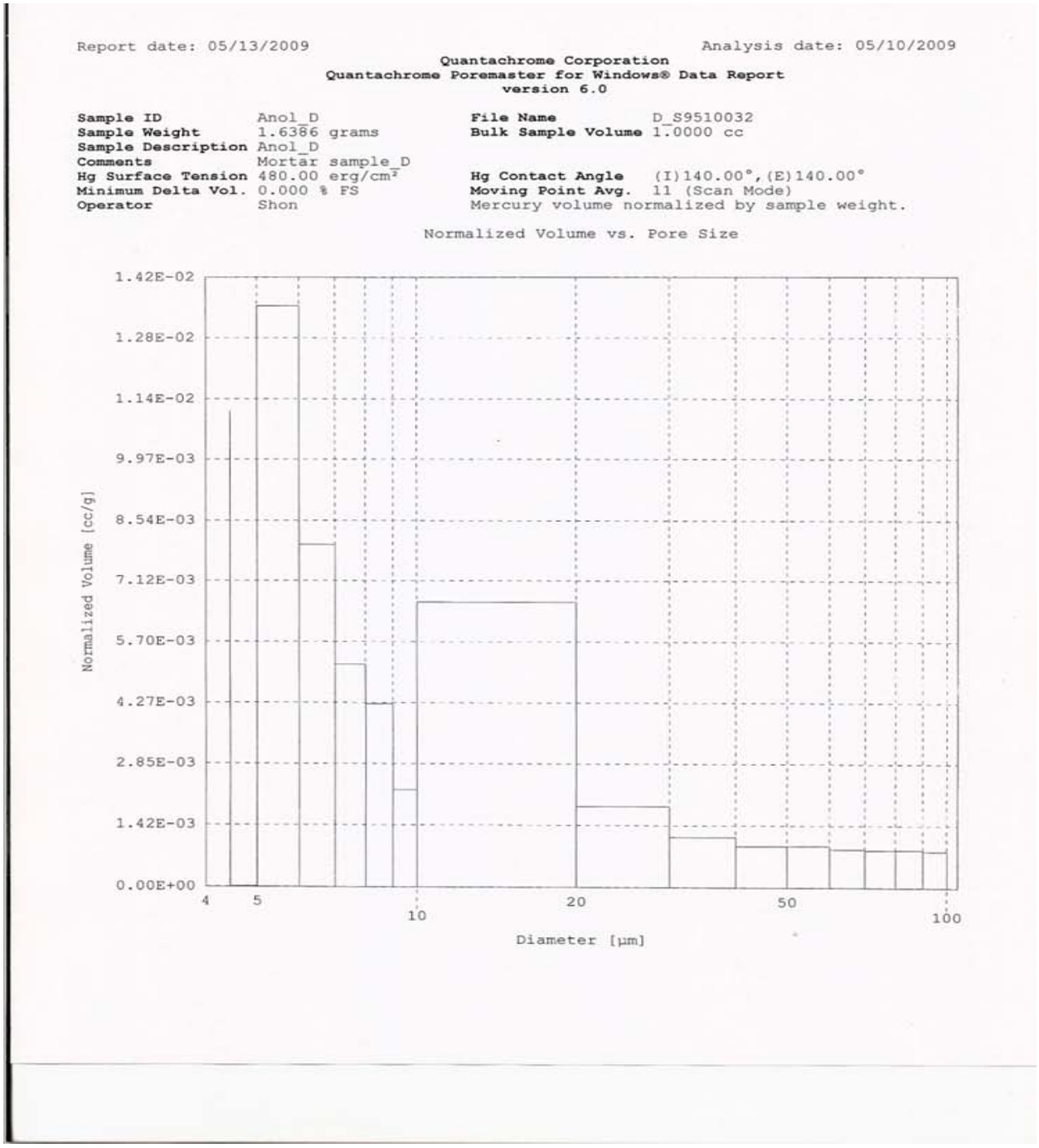

Figure 24. Normalized volume vs. pore size diameter for 120 ^{o}F sample

SEM Analysis

Qualitative Porosity Analysis of Heated Rebar Samples

In the heated rebar experiment it was discussed how the higher temperature gradient between the heated rebar and the neighboring cement at the rebar-concrete interface, causes faster drying of the interface and predicted poor cement hydration of the interface.

The above explanation can be verified by the use of SEM for qualitative analysis. Figure 25 shows the SEM micrograph for rebar-concrete interface of the sample prepared at 180 ^{o}F. The large number of voids in the sample shows the extent of porosity at the interface which is very high in this sample.

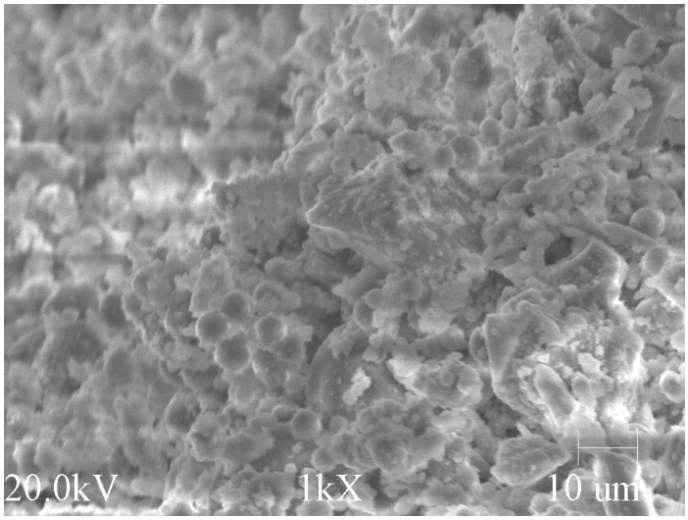

Figure 25. SEM micrograph for rebar-concrete interface of the sample prepared at 180 ^{o}F

Figure 26 shows the SEM micrograph for rebar-concrete interface of the sample prepared at 160 ^{o}F. The number of voids in the micrograph show the extent of porosity at the interface which is high in this sample but less compared to the 180 ^{o}F sample.

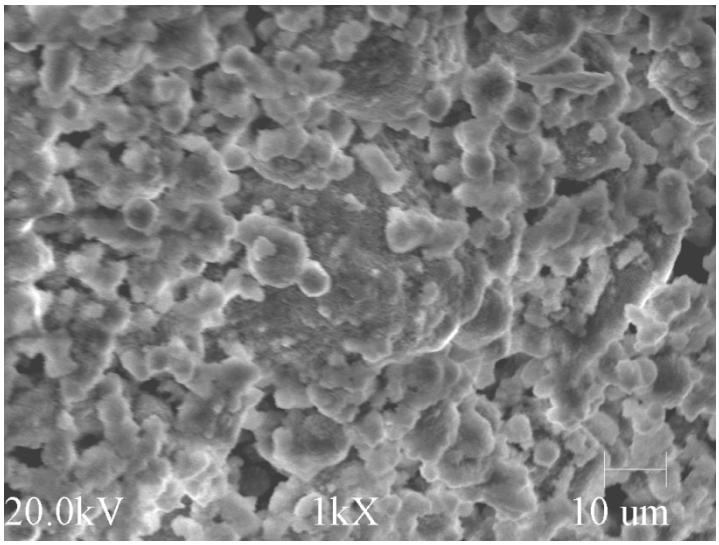

Figure 26. SEM micrograph for rebar-concrete interface of the sample prepared at 160 ^{o}F

Figure 27 shows the SEM micrograph for rebar-concrete interface of the sample prepared at 140 ^{o}F. The lesser number of voids present shows the extent of porosity at the interface which is moderate in this sample but less compared to the 180 ^{o}F sample and almost similar to 160 ^{o}F sample.

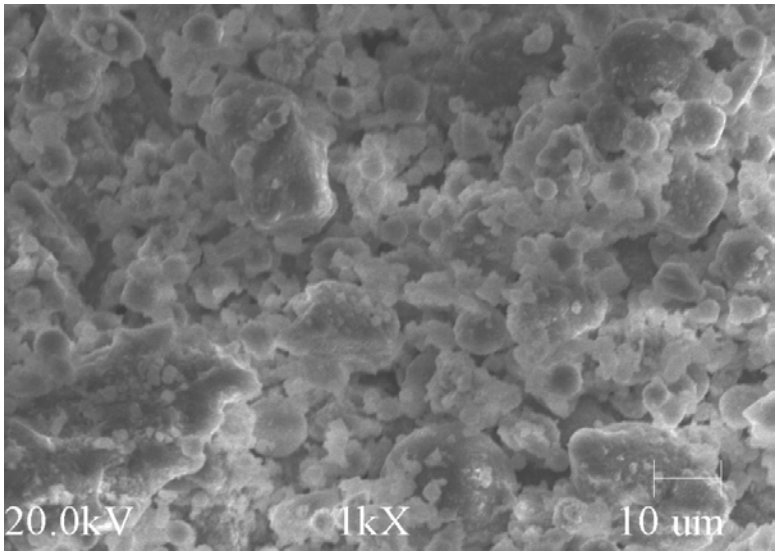

Figure 27. SEM micrograph for rebar-concrete interface of the sample prepared at 140 ^{o}F

Figure 28 shows the SEM micrograph for rebar-concrete interface of the sample prepared at 120 ^{o}F. The few voids present show the extent of porosity at the interface which is very less in this sample as compared to the other three samples.

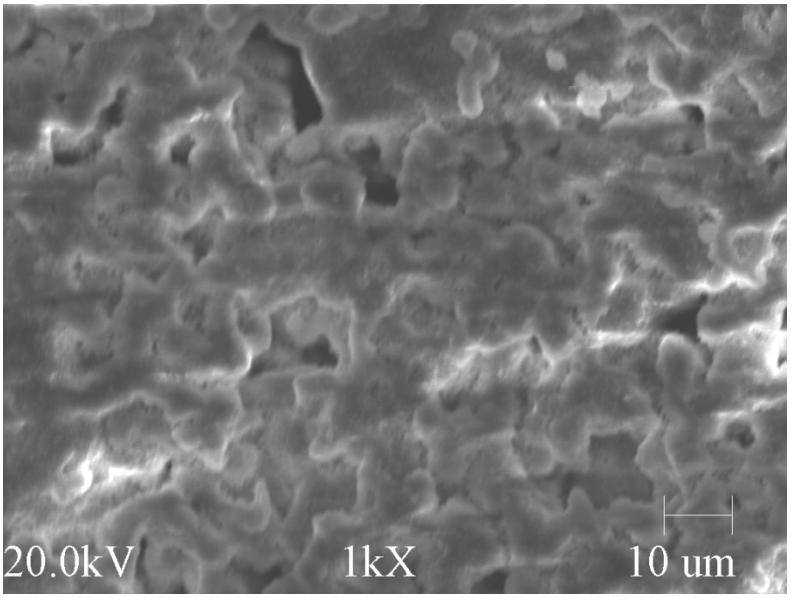

Figure 28. SEM micrograph for rebar-concrete interface of the sample prepared at 120 ^{o}F

Morphological Features of Cast Samples after Fracture

The SEM micrographs of the rebar concrete interface were taken for the fly ash and non fly ash samples that were cast at 77 ^{o}F and 150 ^{o}F with w/c ratio of 0.4 and 0.5. The fly ash samples were compared with the non fly ash ones and significant differences were observed.

The sample set of 28 days was only considered for SEM analysis as the hydration process is complete. The SEM micrographs of samples prepared at 77 ^{o}F with w/c ratio of 0.4 with both non fly ash (a, b) and fly ash (c, d) are shown in the Figure 29 below.

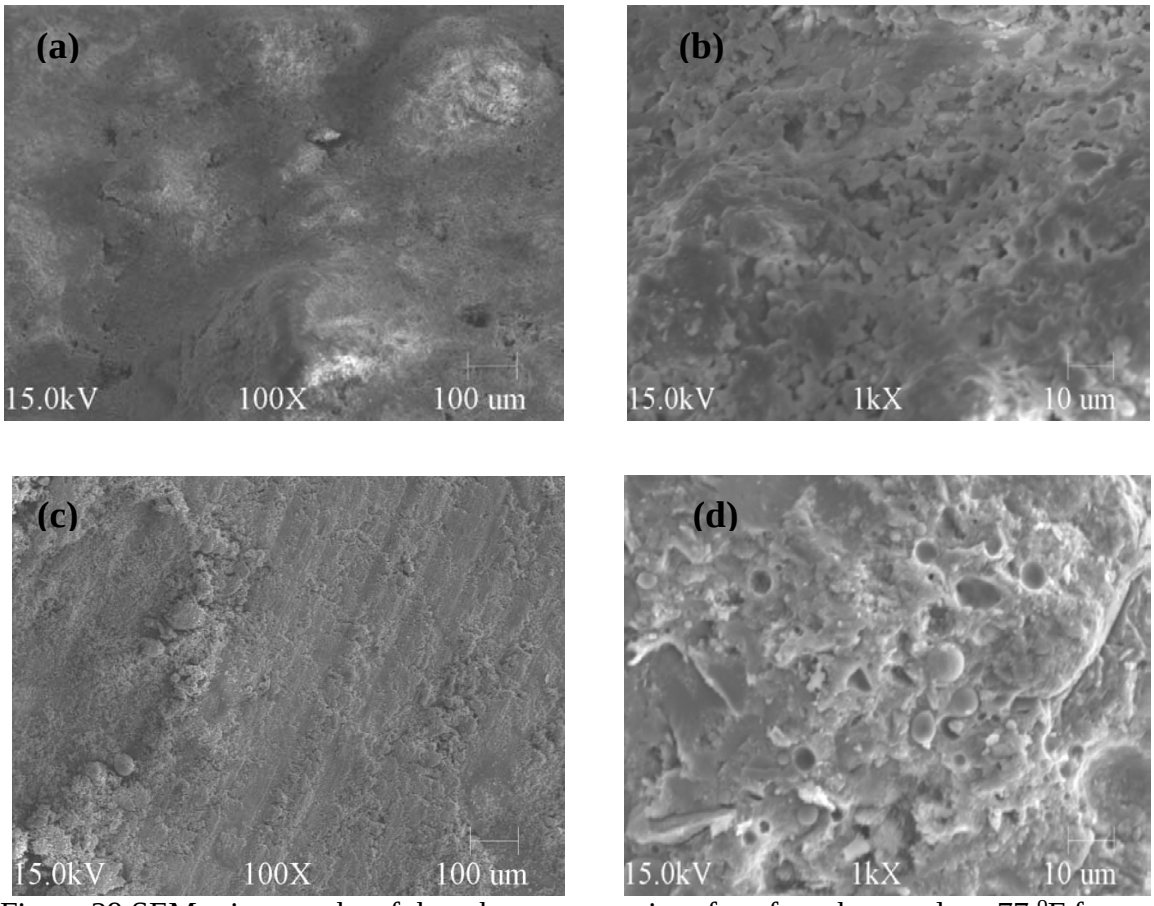

Figure 29.SEM micrographs of the rebar-concrete interface for rebar steels at 77 ^{o}F for w/c 0.40 after 28 days with non fly ash (a,b), and fly ash (c,d).

SEM micrographs for the 28 days set sample without fly ash show extensive porosity which leads to micro-cracks (a, b). The micrographs for the sample containing fly ash (c, d) shows that there is no cracking that takes place and the rebar-concrete interface is less porous in nature. The fly ash (round particles) is shown clearly in the micrographs above which act as stabilizers and improve the bonding between rebar and concrete.

Electron Dispersive X-ray Spectroscopy (EDS) was performed for the 77 ^{o}F and 0.4 w/c sample not containing fly ash (Figure 30) which showed its concrete mix composition and the percentage amount of elements it contained. The calcium peak is the

highest as it is the main constituent of the concrete sample. The gold peak shows the coating done earlier for conduction purpose.

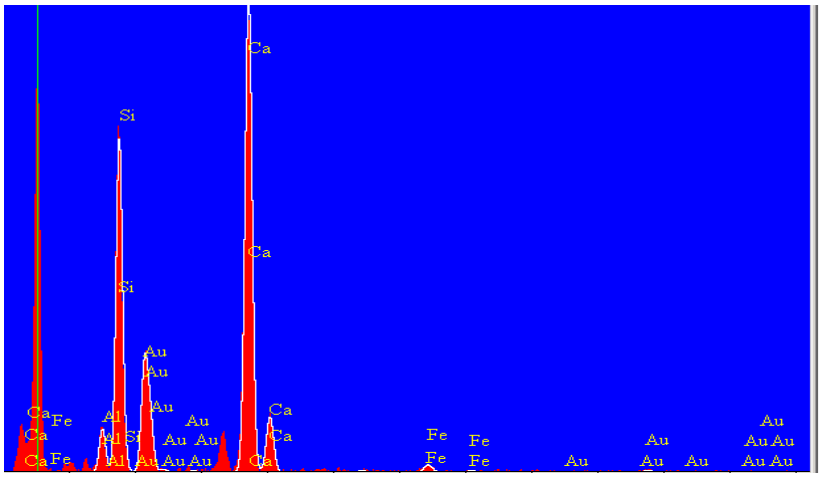

Component	Conc.		
Cr	0.328	wt.%	
Mn	0.161	wt.%	
Ni	0.416	wt.%	
Fe	2.309	wt.%	
Ca	53.489	wt.%	
Al	4.478	wt.%	
Si	25.631	wt.%	
Au	13.188	wt.%	
	100.000	wt.%	Total

Elt.	Line	Intensity (c/s)	Error 2-sig	Atomic %	Conc	
Al	Ka	17.06	0.826	6.540	4.478	wt.%
Si	Ka	133.62	2.312	35.960	25.631	wt.%
Ca	Ka	210.99	2.905	52.589	53.489	wt.%
Cr	Ka	0.71	0.169	0.249	0.328	wt.%
Mn	Ka	0.29	0.108	0.115	0.161	wt.%
Fe	Ka	3.55	0.377	1.630	2.309	wt.%
Ni	Ka	0.42	0.129	0.279	0.416	wt.%
Au	La	0.87	0.187	2.638	13.188	wt.%
				100.000	100.000	wt.%

kV	15.0
Takeoff Angle	45.0°
Elapsed Livetime	100.0

Figure 30. EDS elements spectrum for the SEM micrograph of the rebar-concrete interface for non fly ash concrete sample at 77 ^{o}F and w/c 0.40 after 28 days.

EDS was also performed for the 77 ^{o}F and 0.4 w/c sample containing fly ash (Figure 31) which showed its concrete mix composition and the percentage amount of elements it contained. The content of Calcium and Silicon is comparatively less possibly due to addition of fly ash.

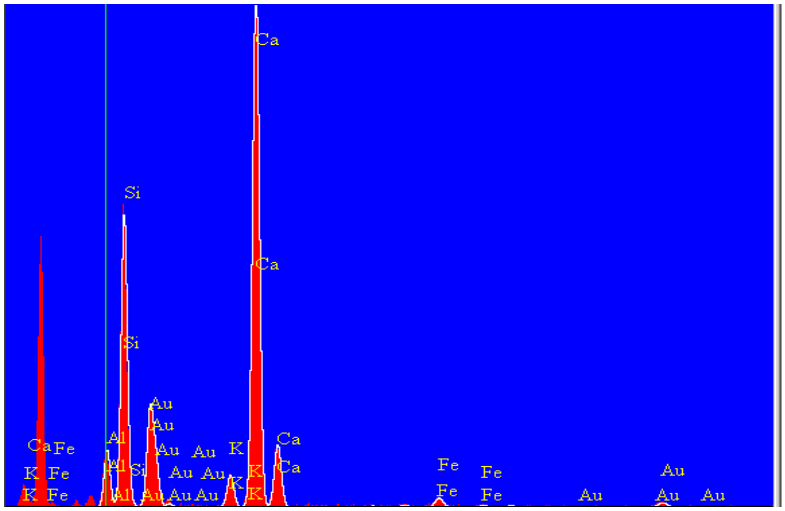

Component	Conc.		
Cr	0.195	wt.%	
Mn	0.354	wt.%	
Ni	0.537	wt.%	
Fe	2.234	wt.%	
Ca	46.085	wt.%	
Si	17.303	wt.%	
Al	4.606	wt.%	
Au	26.342	wt.%	
K	2.343	wt.%	
	100.000	wt.%	Total

Elt.	Line	Intensity (c/s)	Error 2-sig	Atomic %	Conc	
Al	Ka	21.15	0.920	7.797	4.606	wt.%
Si	Ka	110.16	2.099	28.136	17.303	wt.%
K	Ka	13.11	0.724	2.737	2.343	wt.%
Ca	Ka	219.90	2.966	52.513	46.085	wt.%
Cr	Ka	0.53	0.146	0.171	0.195	wt.%
Mn	Ka	0.81	0.180	0.294	0.354	wt.%
Fe	Ka	4.33	0.416	1.827	2.234	wt.%
Ni	Ka	0.68	0.165	0.418	0.537	wt.%
Au	La	2.23	0.298	6.108	26.342	wt.%
				100.000	100.000	wt.%

kV	15.0
Takeoff Angle	45.0°
Elapsed Livetime	100.0

Figure 31. EDS elements spectrum for the SEM micrograph of the rebar-concrete interface for fly ash concrete sample at 77 ^{o}F and w/c 0.40 after 28 days.

The second set of SEM micrographs are for samples prepared at 77 ^{o}F with w/c ratio of 0.5 with both non fly ash (a, b) and fly ash (c, d) are shown in the Figure 32 below.

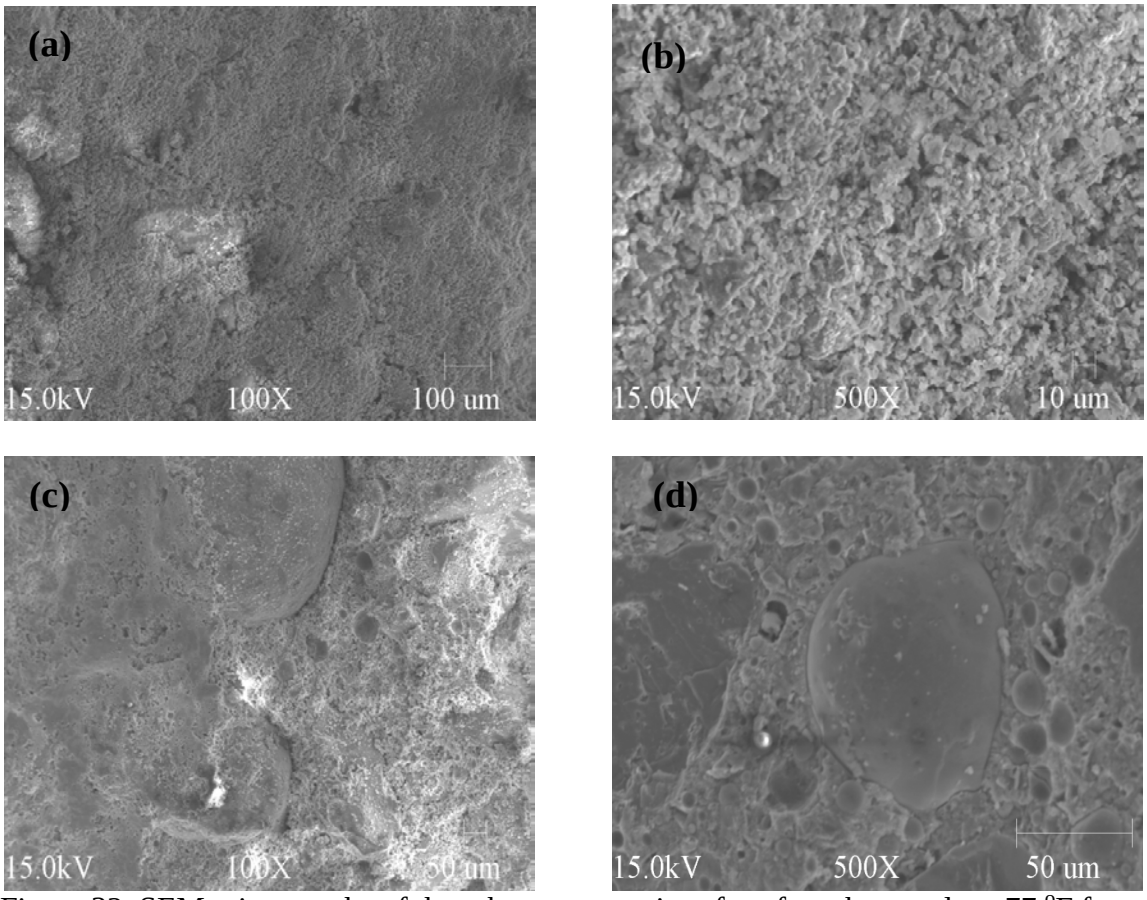

Figure 32. SEM micrographs of the rebar-concrete interface for rebar steels at 77 ^{o}F for w/c 0.50 after 28 days with non fly ash (a,b), and fly ash (c,d).

Higher water to cement ratio appears to have resulted in the formation of more porous concrete (a-d). When w/c was increased to 0.50, the extent of porous rebar-concrete interface region also increased which lead to the formation of micro-cracks which are clearly visible in non-fly ash samples. Figure 32 (a, b) show the crack propagation taking place and this is in agreement with field observations. The micrographs for the sample containing fly ash (c, d) shows that there is no cracking that

takes place and the rebar-concrete interface is comparatively less porous in nature. The fly ash particles are shown clearly in the micrographs above which increase the fluidity of fresh concrete, representing the water reducing effect.

EDS was performed for the 77 ^{o}F and 0.5 w/c samples not containing fly ash (Figure 33) which showed its concrete mix composition and the percentage amount of elements it contained. The calcium peak is the highest as it is the main constituent of the concrete sample. The gold peak shows the coating done earlier for conduction purpose.

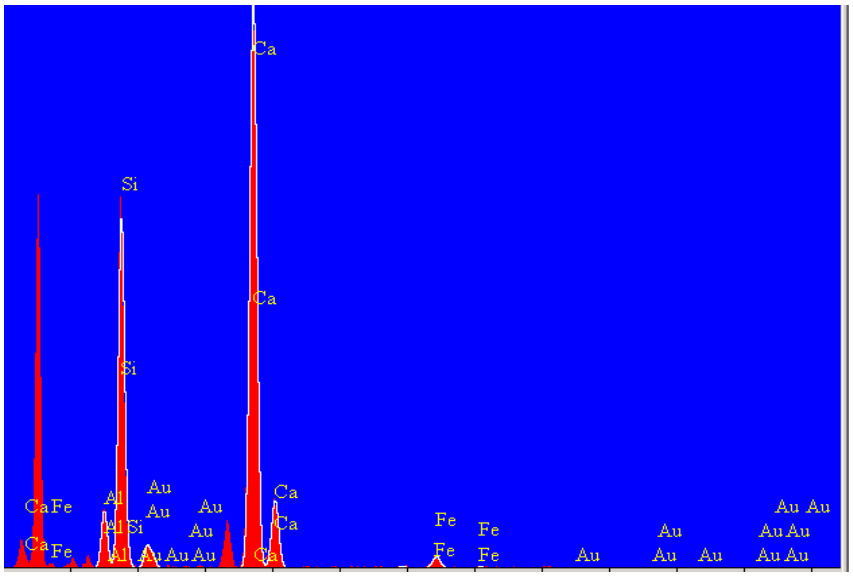

Component	Conc.		
Cr	0.150	wt.%	
Mn	0.450	wt.%	
Ni	0.173	wt.%	
Al	5.557	wt.%	
Si	25.165	wt.%	
Au	5.095	wt.%	
Fe	3.556	wt.%	
Ca	59.853	wt.%	
	100.000	wt.%	Total

Elt.	Line	Intensity (c/s)	Error 2-sig	Atomic %	Conc	
Al	Ka	36.05	1.201	7.631	5.557	wt.%
Si	Ka	222.63	2.984	33.198	25.165	wt.%
Ca	Ka	411.68	4.058	55.333	59.853	wt.%
Cr	Ka	0.56	0.149	0.107	0.150	wt.%
Mn	Ka	1.39	0.236	0.304	0.450	wt.%
Fe	Ka	9.25	0.608	2.359	3.556	wt.%
Ni	Ka	0.29	0.108	0.109	0.173	wt.%
Au	La	0.57	0.150	0.959	5.095	wt.%
				100.000	100.000	wt.%

kV	15.0
Takeoff Angle	45.0°
Elapsed Livetime	100.0

Figure 33. EDS for the SEM micrograph of the rebar-concrete interface for non fly ash concrete sample at 77 ^{o}F and w/c 0.50 after 28 days.

EDS was also performed for the 77 ^{o}F and 0.5w/c sample containing fly ash which showed its concrete mix composition and the percentage amount of elements it contained (Figure 34).

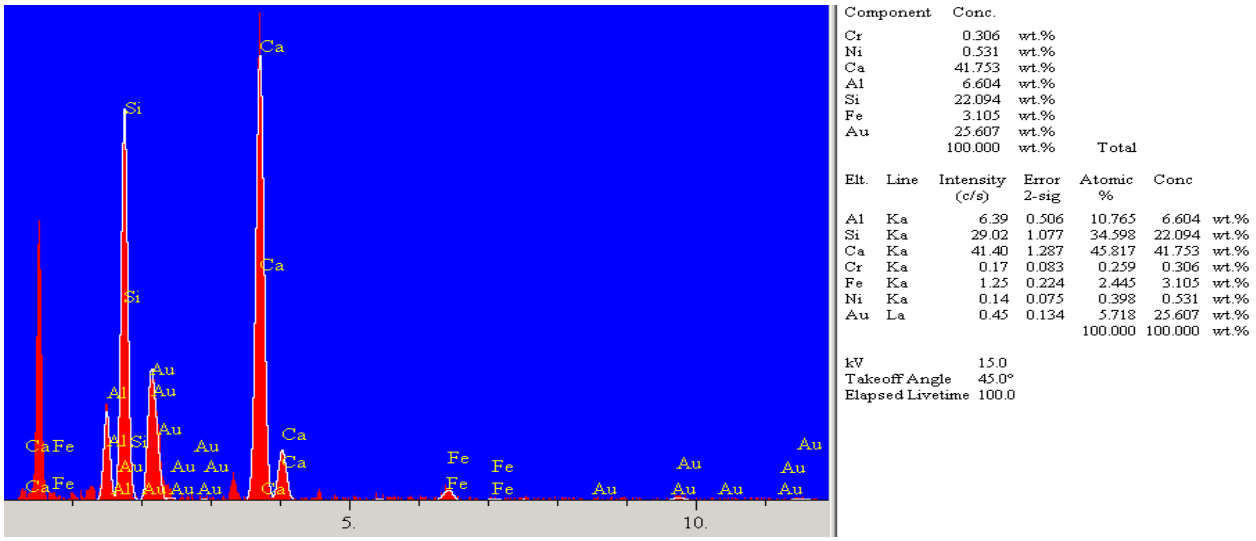

Figure 34. EDS for the SEM micrograph of the rebar-concrete interface for fly ash concrete sample at 77 ^{o}F and w/c 0.50 after 28 days.

The third set of SEM micrographs are for samples prepared at 150 ^{o}F with w/c ratio of 0.4 with both non fly ash (a, b) and fly ash (c, d)) are shown in Figure 35 below.

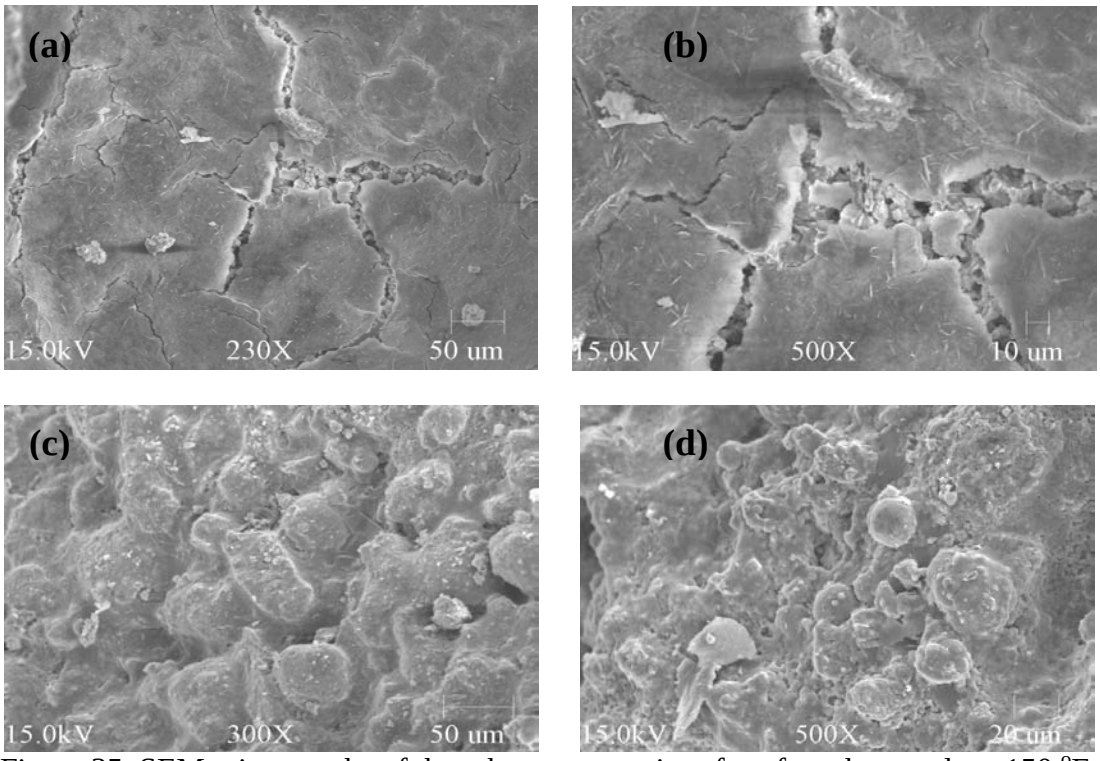

Figure 35. SEM micrographs of the rebar-concrete interface for rebar steels at 150 ^{o}F for w/c 0.40 after 28 days with non fly ash (a,b), and fly ash (c,d).

Lack of solid bond formation between aggregates rich region for non fly ash sample near the rebar is show in Figure 35 (a, b). These poorly bonded aggregate particles add a new level of concrete heterogeneity and disrupt the packing of cement particles locally at the cement paste aggregate interface. Micro-crack formation along the rebar length is also shown in Figure 35 (a, b). The micrographs for the sample containing fly ash (c, d) shows that there is no cracking that takes place and the rebar-concrete interface is comparatively less porous in nature. The fly ash particles are shown clearly in the micrographs above which act as stabilizers and improve the bonding between rebar and concrete.

EDS was performed for the 150 ^{o}F and 0.4 w/c samples not containing fly ash (Figure 36) which showed its concrete mix composition and the percentage amount of elements it contained. The calcium peak is the highest as it is the main constituent of the concrete sample. The gold peak shows the coating done earlier for conduction purpose.

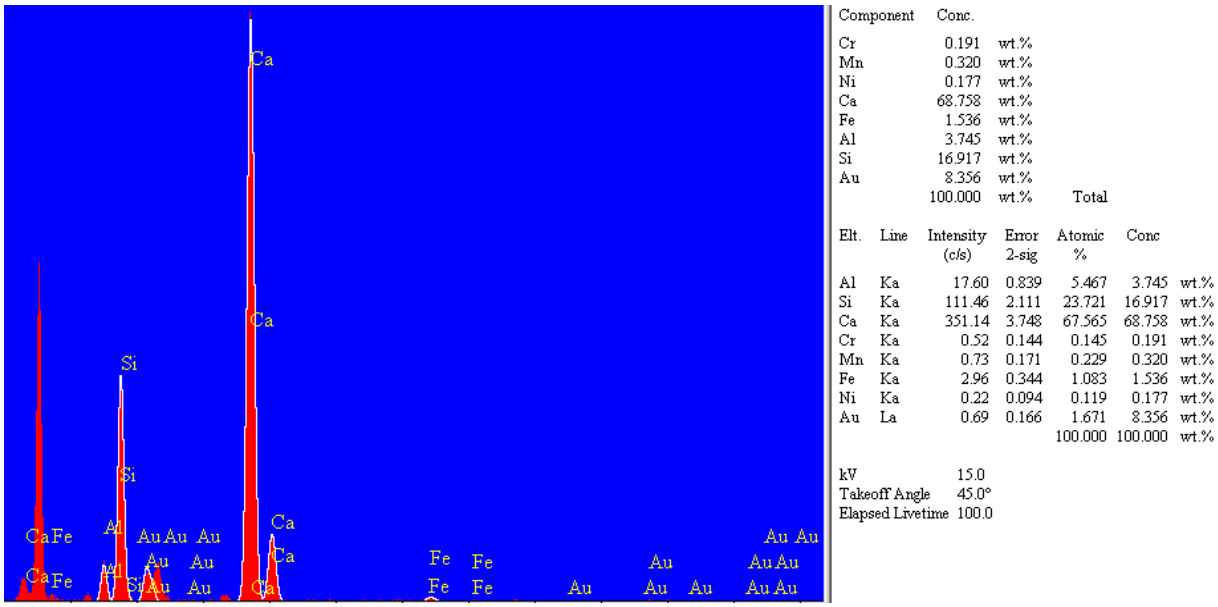

Figure 36. EDS elements spectrum for the SEM micrograph of the rebar-concrete interface for non fly ash concrete sample at 150 ^{o} F and w/c 0.40 after 28 days.

EDS was also performed for the 150 ^{o}F and 0.4w/c sample containing fly ash which showed its concrete mix composition and the percentage amount of elements it contained (Figure 37).

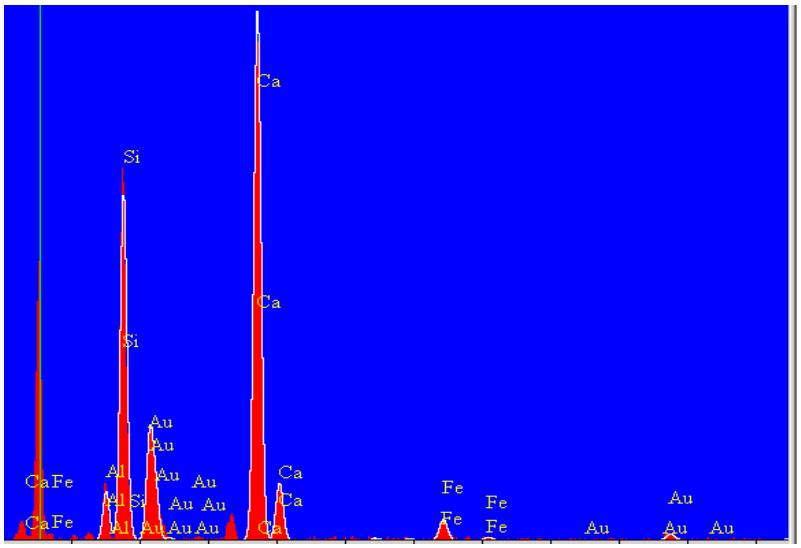

Component	Conc.		
Cr	0.302	wt.%	
Mn	0.249	wt.%	
Ni	0.208	wt.%	
Ca	39.166	wt.%	
Si	17.479	wt.%	
Fe	4.188	wt.%	
Au	35.025	wt.%	
Al	3.384	wt.%	
	100.000	wt.%	Total

Elt.	Line	Intensity (c/s)	Error 2-sig	Atomic %	Conc	
Al	Ka	11.92	0.690	6.297	3.384	wt.%
Si	Ka	86.00	1.855	31.247	17.479	wt.%
Ca	Ka	142.96	2.391	49.065	39.166	wt.%
Cr	Ka	0.65	0.161	0.292	0.302	wt.%
Mn	Ka	0.45	0.134	0.228	0.249	wt.%
Fe	Ka	6.35	0.504	3.765	4.188	wt.%
Ni	Ka	0.21	0.091	0.178	0.208	wt.%
Au	La	2.34	0.306	8.928	35.025	wt.%
				100.000	100.000	wt.%

kV	15.0
Takeoff Angle	45.0°
Elapsed Livetime	100.0

Figure 37. EDS elements spectrum for the SEM micrograph of the rebar-concrete interface for fly ash concrete sample at 150 ^{o} F and w/c 0.40 after 28 days.

The fourth set of SEM micrographs are for samples prepared at 150 ^{o}F with w/c ratio of 0.5 with both non fly ash (Figure 38 (a, b)) and fly ash (Figure 38 (c, d)) are shown in Fig 38 below.

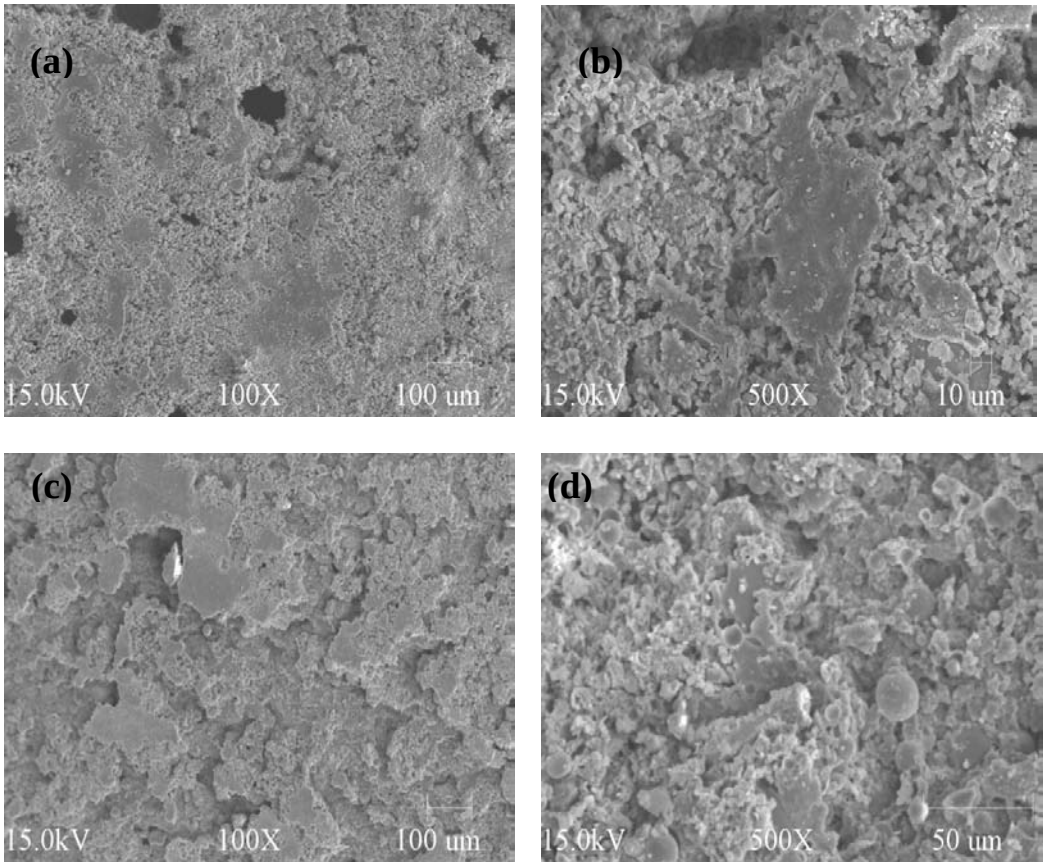

Figure 38. SEM micrographs of the rebar-concrete interface for rebar steels at 150 ^{o}F for w/c 0.50 after 28 days with non fly ash (a,b), and fly ash (c,d).

Higher water to cement ratio appears to have resulted in the formation of more porous concrete Figure 38 (a-d). Lack of solid bond formation between aggregates rich region for non fly ash sample near the rebar is shown in Figure 38 (a, b). These poorly bonded aggregate particles add a new level of concrete heterogeneity and disrupt the packing of cement particles locally at the cement paste aggregate interface. Figure 38 (a, b) shows a region highly concentrated with fraction of mm size voids possibly indicating fast evaporation and bubble formation thus preventing strong bond formation between rebar and concrete. As the w/c ratio increases; the porosity in the rebar-concrete interface is also increased, resulting in the initiation and development of microcracks in this zone.

The existence of these cracks are detrimental to the concrete bond strength because when they coalesce and reach the surface, they allow for the chloride ingress into the concrete structure which will ultimately result in the formation of expansive corrosion products (rust) which occupy several times the volume of the original steel consumed. The micrographs for the sample containing fly ash Figure 38 (c, d) shows that there is no cracking that takes place and the rebar-concrete interface is comparatively less porous in nature. The fly ash particles are shown clearly in the micrographs above which act as stabilizers and improve the bonding between rebar and concrete.

EDS was performed for the 150 ^{o}F and 0.5 w/c samples not containing fly ash (Figure 39) which showed its concrete mix composition and the percentage amount of elements it contained. The calcium peak is the highest as it is the main constituent of the concrete sample. The gold peak shows the coating done earlier for conduction purpose.

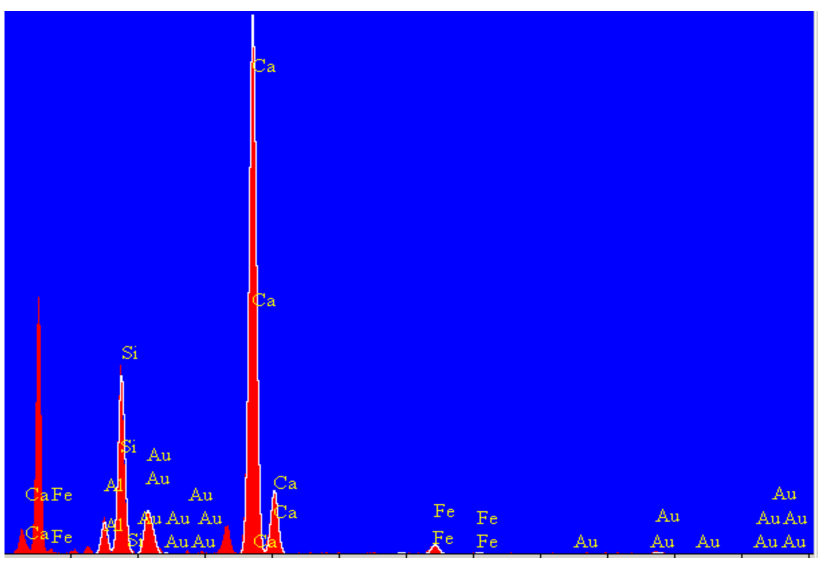

Component	Conc.	
Cr	0.222	wt.%
Mn	0.390	wt.%
Ni	0.209	wt.%
Ca	60.699	wt.%
Fe	3.065	wt.%
Al	3.526	wt.%
Si	14.036	wt.%
Au	17.853	wt.%
	100.000	wt.% Total

Elt.	Line	Intensity (c/s)	Error 2-sig	Atomic %	Conc	
Al	Ka	19.16	0.876	5.668	3.526	wt.%
Si	Ka	107.62	2.075	21.677	14.036	wt.%
Ca	Ka	357.80	3.783	65.694	60.699	wt.%
Cr	Ka	0.72	0.170	0.185	0.222	wt.%
Mn	Ka	1.06	0.206	0.308	0.390	wt.%
Fe	Ka	7.05	0.531	2.381	3.065	wt.%
Ni	Ka	0.31	0.112	0.154	0.209	wt.%
Au	La	1.78	0.267	3.932	17.853	wt.%
				100.000	100.000	wt.%

kV 15.0
Takeoff Angle 45.0°
Elapsed Livetime 100.0

Figure 39. EDS elements spectrum for the SEM micrograph of the rebar-concrete interface for non fly ash concrete sample at 150 ^{o}F and w/c 0.50 after 28 days.

EDS was also performed for the 150 ^{o}F and 0.5w/c sample containing fly ash which showed its concrete mix composition and the percentage amount of elements it exactly contained (Figure 40).

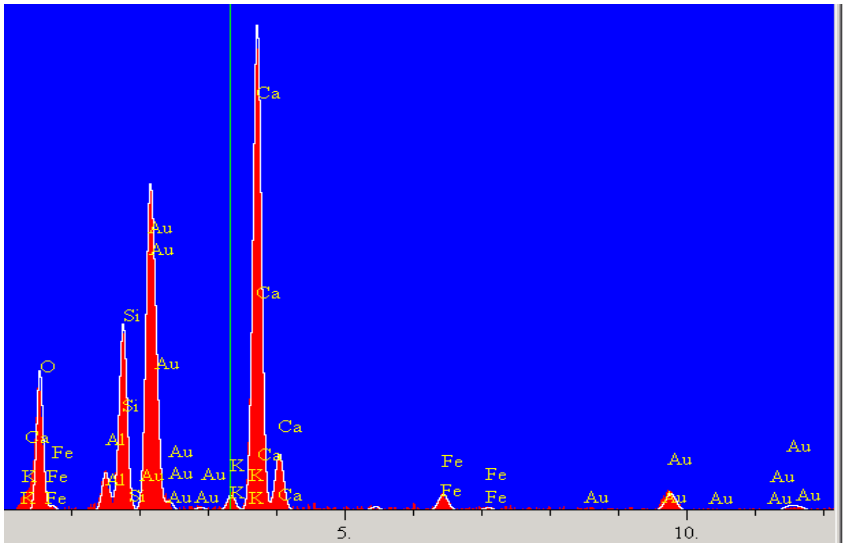

Component	Conc.		
Cr2O3	66.047	wt.%	
NiO	33.952	wt.%	
Al	0.000	wt.%	
Si	0.000	wt.%	
Ca	0.000	wt.%	
Fe	0.000	wt.%	
Au	0.000	wt.%	
K	0.000	wt.%	
	100.000	wt.%	Total

Elt.	Line	Intensity (c/s)	Error 2-sig	Atomic %	Conc	
O	Ka	30.72	1.109	57.048	28.128	wt.%
Al	Ka	9.95	0.631	0.000	0.000	wt.%
Si	Ka	48.49	1.393	0.000	0.000	wt.%
K	Ka	4.50	0.424	0.000	0.000	wt.%
Ca	Ka	144.28	2.402	0.000	0.000	wt.%
Cr	Ka	1.10	0.209	28.201	45.190	wt.%
Fe	Ka	5.37	0.464	0.000	0.000	wt.%
Ni	Ka	0.42	0.129	14.751	26.682	wt.%
Au	La	6.40	0.506	0.000	0.000	wt.%
				100.000	100.000	wt.%

kV	15.0
Takeoff Angle	45.0°
Elapsed Livetime	100.0

Figure 40. EDS elements spectrum for the SEM micrograph of the rebar-concrete interface for fly ash concrete sample at 150 ^{o} F and w/c 0.50 after 28 days.

Because fly ash particles are small, they effectively fill voids. They are hard and round and have a “ball bearing” effect that allows concrete to be produced using less water. Both characteristics contribute to enhanced concrete workability and durability. According to Headwaters Resources-fly ash for concrete broacher the main advantages of fly ash addition to concrete are:

1) Fly ash combines with free lime, increasing compressive strength over time.
2) Increased density and long term pozzolanic action of fly ash, which ties up free lime, results in fewer bleed channels and decreases permeability.

3) By decreasing concrete permeability, fly ash can reduce the rate of ingress of water, corrosive chemicals and oxygen — thus protecting steel reinforcement from corrosion and its subsequent expansive result.
4) Dense fly ash concrete helps keep aggressive compounds on the surface, where destructive action is lessened. Fly ash concrete is also more resistant to attack by sulfate, mild acid, soft (lime hungry) water, and seawater.
5) The largest contributor to drying shrinkage is water content. The lubricating action of fly ash reduces water content and drying shrinkage.
6) Concrete made with fly ash will be slightly lower in strength than straight cement concrete up to 28 days, equal strength at 28 days, and substantially higher strength within a year's time.
7) Fly ash reduces the amount of cement needed in the mix to produce workability. Because fly ash creates more paste, and by its shape and dispersive action makes the paste more "slippery", the amount of cement proportioned into the mix can be reduced. Since cement has a much greater surface area than larger aggregates and therefore requires more paste, reducing the cement means the paste available can more efficiently coat the surface area of the remaining aggregates.

CHAPTER 5

CONCLUSIONS AND RECOMMENDATIONS

The outcome of this research was that as the rebar temperature, at the time of concrete placement increases, the pore volume at the rebar-concrete interface also increases and the pullout force that the concrete can withstand decreases.

The aim of this research was to show the improved bonding with the inclusion of fly ash at lower rebar temperature with a lower w/c ratio would be expected to resist horizontal cracking which could be potentially caused due to porosity at the rebar-concrete interface. This was proved quantitatively using pullout tests and also qualitatively using SEM and EDS analysis at the interface of the fly ash and control non fly ash samples.

Rebar temperature was proven to affect cement pore density and pore size distribution affecting rebar-cement bonding quality. This research proves that porosity at the rebar-concrete interface is directly proportional to the rebar temperature at the time of concrete pouring. This was proved using tests such as MIP for quantitative analysis and FTIR for qualitative analysis. The SEM analysis also showed the porous nature of the samples at micro level.

As the result of this investigation and based on the test data, following conclusions can be made:

1. All fly ash containing samples showed higher pullout strength compared to no fly ash containing samples. SEM results show more cracks on non fly ash containing concrete surfaces while fly ash containing surface showed cohesive and uniform cement morphology with relatively less cracks and fractures.
2. EDS results of both fly ash containing as well as control samples showed typical constituents of concrete including compounds of Si, Al, Ca, etc.
3. Heated rebar steels causes partial drying of concrete at the rebar concrete interface. Absorption band at wave number of 3450 cm^{-1} associated with water content of cement phase in the FTIR spectra showed highest intensity for the lowest rebar surface temperature.
4. Partial drying of the cement or concrete at the rebar-cement interface produces a lower w/c ratio at the interface as compared to bulk cement w/c ratio. Such a difference in w/c ratio potentially causes incomplete hydration leading to poor bonding between rebar and cement. This leads to low pullout strength.
5. High rebar surface temperatures produced higher amounts of cement porosity at the interface as indicated by mercury intrusion porosimetry results. Higher rebar surface temperatures also formed larger pore diameters in the cement located at the rebar-cement interface.
6. Samples with higher the w/c ratio showed lower pullout strength. Combination of high w/c ratio and high rebar surface temperature resulted in the lowest pullout strength.

Based on the results of this research, I recommend including the effects of rebar temperature at the time of concrete placement in the TxDOT Pavement Design Guide for CRCP construction practices. Determination of the specific temperature beyond which avoiding concrete placement is advisable needs to be specified in a future study. However, the rebar temperature effect on CRCP cracking deserves a proper attention.

REFERENCES

[1]. A.B. Abell, K.L. Willis and D.A. Lange, "Mercury intrusion porosimetry and micrograph analysis of cement-based materials," *J. Colloid Interface Sci*, vol. 211, pp. 39-44, March 1999.

[2]. Oner, S. Akyuz, R. Yildiz, "An experimental study on strength development of concrete containing fly ash and optimum usage of fly ash in concrete," *Cement and Concrete Research* vol.35, pp.1165-1171, June 2005.

[3]. Amnon Katz, Neta Berman, "Modeling the effect of high temperature on the bond of FRP reinforcing bars to concrete," *Cement and C oncrete C omposites* vol.22, pp. 433-44, June 2000.

[4]. American Society of Testing and Materials (ASTM) Standard (2001). *ASTM Standard A615: Standard Specification for Deformed and P lain B illet-Steel B ars for Concrete Reinforcement,* Pennsylvania.

[5]. American Society of Testing and Materials (ASTM) Standard (2009), *Standard B 962-08, Standard Test Methods for Density of Compacted or Sintered Powdered Metallurgy (PM) Products Using Archimedes' Principle,* Pennsylvania.

[6]. American Society of Testing and Materials (ASTM) Standard (2001), *Standard C39/C 39M -01, Standard T est M ethod f or c ompressive s trength of cylindrical concrete specimens,* Pennsylvania.

[7]. American Society of Testing and Materials (ASTM) Standard (2001), *Standard C 192/C 192M -00, Standard P ractice f or Making and C uring C oncrete T est Specimens in the Laboratory,* Pennsylvania.

[8]. Abdolkarim Abbasi, Paul J. Hogg, "Temperature and environmental effects on glass fiber rebar: modulus, strength and interfacial bond strength with concrete." *Composites: Part B* vol.36, pp.394 – 404, July 2005.

[9]. B. A. Dockter and D. M. Jagiella, "Engineering and Environmental Specifications of State Agencies for Utilization and Disposal of Coal Combustion Products," presented at the World of Coal Ash Conference, Lexington Kentucky, April 11-15, 2005.

[10]. B. Bourdette, E. Ringot, J.P. Ollivier, “Modelling of the transition zone porosity,” *Cement and Concrete Research* vol.25, pp.741-751,April 1995.

[11]. Bertolini L, Elsener B, Pedeferri P, Polder R, “Corrosion of steel in concrete,” *J. Corrosion Sci*, vol.47, pp.3019-3033, Dec 2005.

[12]. John Cairns, Voula Pantazopoulou, Keivan Noghabai, Jesus Rodriguez, “Bond of Reinforcement in concrete,” International Federation for Structural Concrete, Switzerland, State of the art report, Bulletin no. 10, pp. 188-215, 2000.

[13]. C. Estakhri, D. Saylak, and S. D. Mohidekar, “Potential for Reduced Greenhouse in Texas Through the Use of High Volume Fly Ash,” Texas Transportation Institute, Collegestation, Texas, SWUTC/04/167709-1, March 2004.

[14]. C. Shi, and J. Qian, “High Performance Cementing Materials from Industrial Slags-a Review,” *Resources, C onservation and R ecycling* vol.29, pp.195-207, 2000.

[15]. E.W. Washburn, “Proceedings of the National Academy of Sciences, PNASA," *Pavement Design G uide, T exas D epartment of T ransportation*, Vol.7, p.115, Revised Oct 2006.

[16]. Elfino, M., Ozyildirim, C., and Steele, R., “CRCP in Virginia, Lessons Learned,” Presented at Fifth International Conference on Concrete Pavement Design and Rehabilitation, Orlando, Florida. Sept 9-13, 2001

[17]. G. F. Vogit, “Early Cracking of Concrete Pavement-Causes and Repairs”, presented at Federal Avaiation Administration Airport Technology Transfer Conference, May May 2, 2002.

[18]. Jeuffroy Georges and Sauterey Raymond, *Cement and Concrete Pavements*. Brookfield, NJ: A.A. Balkema Publishers, 1996.

[19]. Headwaters Resources (2005), Fly Ash for concrete brochure, Utah. [Online]. Available: http://www.flyash.com/data/upimages/press/HWR_brochure_flyash.pdf.

[20]. IBP Fraunhofer (May 2001), Mercury Intrusion Porosimetry, Stuttgart, Germany. [Online]. Available: http://www.hoki.ibp.fhg.de/wufi/grundl_poros_e.html.

[21]. J.G. Laguros, D. Ross, M. Baker, “Fly Ash Concrete: A Study of the Reaction Products Using X-ray Diffraction and SEM”, ODOT Study No. 82-01-2, ORA 155-088, Aug 1984.

[22]. Jeong-Hee Nam, "Early-Age behavior of CRCP and its implications for long-term Performance," PhD. Thesis Dissertation, Dept. Civil. Engg, University of Texas at Austin, 2005.

[23]. John P Broomfield, *Corrosion of steel in concrete,* New York Wiley, 1997,

[24]. Kim, S. and Won, M, " Horizontal cracking in continuously reinforced concrete pavements," *ACI Structural Journal* pp.784-791, Nov 2004.

[25]. Kosmatka, S.H., and Panarese, W.C, "Design and Control of Concrete Mixtures," presented at 13th ed. Portland Cement Association, Skokie, IL, 1988.

[26]. L. Dongxu, W. Xuequan, S. Jinlin, and W. Yujiang, "The Influence of Compound Admixtures on the Properties of High-content Slag Cement," *Cement and Concrete Research*, vol.30, pp. 45-50, 2000.

[27]. L.G. Archuleta, Jr., P.J. Tikalsky and R.L. Carrasquillo, "Production of Concrete Containing Fly Ash for Structural Applications," University of Texas At Austin, Research Report CTR-3-9-84-364-1, May 1986.

[28]. Laurence M. Harwood, Christopher J. Moody. "Experimental organic chemistry: Principles and Practice" (Illustrated ed), pp. 292, 1989.

[29]. M.M. Jalili, S. Moradian, D. Hosseinpour, "The use of inorganic conversion coatings to enhance the corrosion resistance of reinforcement and the bond strength at the rebar/concrete," *J. Construction and B uilding M aterials* Volume.23, 2006.

[30]. M. Mouret, A. Bascoul, and G. Escadeillas, "Microstructural features of Concrete in Relation to Initial Temperature-SEM and ESEM Characterization", *Cement and Concrete Research*, vol.29, pp.369-375, March 1999.

[31]. Md. Safiuddin and Nataliya Hearn, "Comparision of ASTM saturation techniques for measuring the permeable porosity of concrete," *Cement and Concrete Research,* vol.35, pp.1008-1013, May 2005.

[32]. P. Stutzmann, "Scanning Electron Microscopy Imaging of Hydraulic Cement Microstructure," *Cement & Concrete Composites*, vol.26, pp.957-966, 2004.

[33]. *Pavement D esign Guide,* Austin, Texas: Texas Department of Transportation, Revised Oct 2006.

[34]. R. Romagnoli, R.O. Batik, V.F. Vetere, J.D. Sota, I.T. Lucchini, R.O. Carbonari, "The influence of the cement paste microstructure on corrosion and the adherence

of reinforcing bars as a function of the water-cement ratio," *Anti-Corrosion Methods and Materials,* vol.49, Issue 1, pp 11-18, 2002.

[35]. R. Siddique, "Effects of Fine Aggregate Replacement with Class F Fly Ash on the Mechanical Properties of Concrete," *Cement and concrete Research*, vol.33, (4), pp.539-547, 2003.

[36]. Robinson C, Beg M A, Dossey T, Hudson W R, "Distress prediction models for rigid pavements for Texas pavement management information system," *Pavement Management Systems for Streets, Highways, and Airports*, Transportation Research Board, Issue no: 1524, Oct 1996.

[37]. S. Nasrazadani and E. Sudoi, "Factors influencing concrete-rebar bond failures in continually reinforced concrete pavements," presented at 88th annual conference of Transportation Research Board of the National Academies, Washington DC, paper No.09-0764, 2009.

[38]. S. Nasrazadani, "Horizontal Cracking in Concrete Pavements," *TxDOT Project No. 0-5549*, Feb 2008.

[39]. Samarai, M., Popovics, S., and Malhotra, V.M., "Effect of High Temperatures on the Properties of Hardened concrete," Transportation Research Record No. 924, 1983.

[40]. Seongcheol Choi and Moon Won, "Horizontal Cracking in Portland Cement Concrete Pavements: Literature Review," *TxDOT Project No. 0-5549*, Feb 2008

[41]. Sidney Diamond, "Considerations in micrograph analysis as applied to investigation of the ITZ in concrete", *Cement and Concrete Composites, vol.* 23, pp.171 – 178, 2001.

[42]. Sidney Diamond, Jingdong Huang, "The ITZ in concrete – a different view based on micrograph analysis and SEM observations", *Cement and Concrete Composites*, vol. 23, pp.179 – 188, 2001.

[43]. Suh, Y.C., Hankins, K., and McCullough, B.F., "Early-Age Behavior of Continuously Reinforced Concrete Pavement and Calibration of the Failure Prediction Model in the CRCP-7 Program," Research Report 1244-3, Center for Transportation Research, The University of Texas at Austin, March 1992.

[44]. Sun Wei, Yan Handong and Zhan Binggen, "Analysis of Mechanism on water-reducing effect of fine ground slag, high-calcium fly ash, and low-calcium fly ash", *Cement and Concrete Research*, vol.33, pp. 1119-1125, Aug 2003.

[45]. Tulin Akcaoglu, Mustafa Tokyay, Tahir Celik, "Assessing the ITZ microcracking via scanning electron microscope and its effect on the failure behavior of concrete", *Cement and Concrete Research, vol.*35, pp.358 – 363, Feb 2005.

[46]. W. Xuequan, Z. Hong, H. Xinkai, and L. Husen, "Study on steel Slag and Fly ash Composite Portland Cement", *Cement and Concrete Research*, vol.29, pp.1103-1106, July 1999.

[47]. X. Fu, etal, "Studies on Blended Cement with a Large Amount of Fly ash", *Cement and Concrete Reseach*, vol.32, 1153-1159, 2002.

[48]. Yunus A. Cengel, "Lumped Systems Analysis", *Heat Transfer – A Practical Approach*, Second Edition, pp.210-211, 2003.